Soft Matter

PAPER

View Article Online
View Journal | View Issue

Check for updates

Cite this: *Soft Matter*, 2022, **18**, 4280

Electric-field-induced oscillations in ionic fluids: a unified formulation of modified Poisson–Nernst–Planck models and its relevance to correlation function analysis

Hiroshi Frusawa

We theoretically investigate an electric-field-driven system of charged spheres as a primitive model of concentrated electrolytes under an applied electric field. First, we provide a unified formulation for the stochastic charge and density dynamics of the electric-field-driven primitive model using the stochastic density functional theory (DFT). The stochastic DFT integrates the four frameworks (the equilibrium and dynamic DFTs, the liquid state theory and the field-theoretic approach), which allows us to justify in a unified manner various modifications previously made for the Poisson–Nernst–Planck model. Next, we consider stationary density–density and charge–charge correlation functions of the primitive model with a static electric field. We predict an electric-field-induced synchronization between emergences of density and charge oscillations. We are mainly concerned with the emergence of stripe states formed by segregation bands transverse to the external field, thereby demonstrating the following: (i) the electric-field-induced crossover occurs prior to the conventional Kirkwood crossover without an applied electric field, and (ii) the ion concentration dependence of the decay lengths at the onset of oscillations bears a similarity to the underscreening behavior found by recent simulation and theoretical studies on equilibrium electrolytes. Also, the 2D inverse Fourier transform of the correlation function illustrates the existence of stripe states beyond the electric-field-induced Kirkwood crossover.

Received 23rd December 2021,
Accepted 1st May 2022

DOI: 10.1039/d1sm01811f

rsc.li/soft-matter-journal

Open Access Article. Published on 26 May 2022. Downloaded on 7/19/2025 4:45:38 PM.
This article is licensed under a Creative Commons Attribution-NonCommercial 3.0 Unported Licence.

I. Introduction

Primitive model

Ionic fluids cover a wide range of charged materials, including solvent-in-salt electrolytes, room-temperature ionic liquids (RTILs), various colloidal dispersions, and polyelectrolytes.[1,2] Recently, ionic fluids are increasingly attracting much attention, due to their diverse applications not only in chemistry and biology[1] but also in renewable energy devices such as batteries, supercapacitors, and separation media.[2–4] Here we consider electrolytes, RTILs, and mixtures of oppositely charged colloids under applied electric fields, as examples of symmetric ionic fluids driven by external electric fields. These appear in biological ion channels, micro/nanofluidic devices for environmental and biomedical applications, and electrolyte-immersed porous electrodes for electrochemical applications.[1–4]

Among models of the ionic fluids on target is a primitive model, or a symmetric collection of charged spheres whose cationic and anionic species have equal size and equal but opposite charge. The primitive model under a static electric field, with which we are concerned, has been widely used to explain the structural and dynamical properties of concentrated electrolytes driven by external electric fields in confined geometries.[2,5–7]

Poisson–Nernst–Planck (PNP) model

The Poisson–Nernst–Planck (PNP) model is the standard approach to describe the primitive model with a static electric field applied.[2,5–7] The Nernst-Planck equation, also known as the drift-diffusion equation, treats ionic currents arising from the combination of Fick's law of diffusion due to a concentration gradient and Ohm's law for drift of ions in a gradient of Coulomb potential. The Nernst-Planck equation represents the conservation law:

$$\partial_t n_l(\boldsymbol{r}, t) = -\nabla\cdot\boldsymbol{J}_l(\boldsymbol{r}, t), \tag{1}$$

where $n_l(\boldsymbol{r}, t)$ $(l = 1,2)$ denotes an instantaneous number density of either cations $(l = 1)$ or anions $(l = 2)$ and $\boldsymbol{J}_l(\boldsymbol{r}, t)$ the associated current vector of the l-th ion density. The PNP model considers the coupled set of the Poisson and NP equations by relating $n_l(\boldsymbol{r}, t)$ to the Coulomb interaction potential *via* the Poisson equation.

Laboratory of Statistical Physics, Kochi University of Technology, Tosa-Yamada, Kochi 782-8502, Japan. E-mail: frusawa.hiroshi@kochi-tech.ac.jp

This journal is © The Royal Society of Chemistry 2022

Open Access Article. Published on 26 May 2022. Downloaded on 7/19/2025 4:45:38 PM.
This article is licensed under a Creative Commons Attribution-NonCommercial 3.0 Unported Licence.

Deficiencies of the PNP model

The PNP model provides a basic description of linear response dynamics of dilute electrolytes perturbed from equilibrium. However, the original PNP model takes no account of (i) steric interactions, (ii) ion–ion Coulomb correlations, and (iii) dielectric boundary effects. Hence, the conventional PNP model is insufficient to predict various electrokinetic phenomena when ions are crowded and/or when the ion distributions are spatially inhomogeneous.[5,6]

For example, the PNP model is not relevant to the interfacial electrokinetic phenomena which are found not only in biological ion channels but also in advanced devices for micro/nanofluidic and electrochemical applications.[5,6] Steric effects become significant in either RTILs or thin electric double layers formed at large applied voltages, which, however, are not included in the PNP model.[5–16]

There are also bulk properties for which the PNP model is not valid: inhomogeneous steady states have been reported by theoretical, experimental, and simulation studies in the bulk region of either electrolytes or oppositely charged colloidal mixtures driven by electric fields.[13,17–20] Theoretically, on the one hand, stationary correlation functions of electric-field-driven electrolytes were calculated, suggesting a tendency to form chains of cations and anions in the external field direction at large electric fields.[13] On the other hand, experimental and simulation studies have provided dynamic phase diagrams of steady states including laned, jammed or clogged, and mixed states of oppositely charged particles under DC or AC electric fields.[17,18] It is well known that lane formation of like-charge particles occurs at a high enough field strength along the applied field.[17,18] At the same time, previous studies have observed that bands of like-charge particles are aligned in a direction non-parallel to the applied field direction when the electric-field-driven colloidal mixtures are in jammed or mixed states.[17,18]

Modified PNP models: deterministic case

A variety of modified PNP (mPNP) models have thus been proposed so far; these arise either from semi-phenomenological methods[5–10] or from deterministic density functional theory (DFT).[11,12] The modifications have aimed to complement the above shortcomings given in (i) to (iii) as follows: (i) Steric effects are included by adding a density current, or its associated chemical potential due to non-Coulombic short-range interactions. (ii) Ion–ion Coulomb correlations are taken into account by modified Poisson equations such as higher-order Poisson equation.[21–24] (iii) Dielectric boundary effects are investigated according to a generalized Born theory which evaluates solvation energy from an ionic self-energy.[25]

Some of the results achieved by the deterministic mPNP models are as follows:[5–10] first, for biological ion channels, the numerical results have been found to agree with experimental or simulation data on the ion channel characteristics of selectivity and rectification. Next, for micro/nanofluidics, it has been demonstrated that a coupled set of the mPNP and Navier-Stokes equations is a good descriptor of the interfacial electrokinetic phenomena. These include electro-osmotic flow, streaming current, and ionic conductance in porous media or nanochannels filled with RTILs or concentrated electrolytes of high valence. Then, in terms of renewable energy technologies, the deterministic mPNP models have successfully explained differential capacitance and non-monotonic oscillatory decay of electric double layers at solid-liquid interfaces with large voltages applied to RTILs or concentrated electrolytes.

Modified PNP models: stochastic case

An alternative approach to extend the PNP dynamics to a stochastic process is the stochastic DFT (SDFT).[11,26] In the SDFT, we use the Dean–Kawasaki model[11,26] that contains multiplicative noise by adding a stochastic current in eqn (1). The Dean–Kawasaki equation can be linearized for fluctuating density field around a reference density.[13–15,27,28] The linearized Dean–Kawasaki equation has proved relevant to describe various dynamics. It is an outstanding feature of the linearized SDFT to justify the inclusion of stochastic processes into the PNP model. The stochastic nature allows us to compute correlation functions for density and charge fluctuations around a uniform state.

Recently, the stochastic mPNP models based on the linearized SDFT have provided the following results:[13–16,27,28] First, the linear Dean–Kawasaki equation has formulated ion concentration-dependent electrical conductivity. The obtained expression for conductivity reproduces the Debye–Hückel-Onsager theory and also explains the experimental results on concentrated electrolytes where the Debye–Hückel-Onsager theory breaks down.[13,15,16] It should be noted that we need to use a regularized interaction potential[15] and to introduce hydrodynamic interactions[15,16] for explaining the high-density results;[15] while this paper will justify the use of regularized form from the first principle, consideration of hydrodynamic interactions is beyond our scope. Furthermore, it is found from the analysis of correlation functions that density–density and charge–charge correlations are long-range correlated even in the steady state. The asymptotic decay of the correlation functions exhibits a power-law behavior with a dipolar character, thereby giving rise to a long-range fluctuation-induced force acting on uncharged confining plates.[14]

However, the above three issues (*i.e.*, (i) to (iii) described above) have yet to be fully addressed by the stochastic mPNP models. It should also be remembered that the stochastic mPNP models have been concerned with linear response dynamics from a uniform density distribution and that there have been few systematic studies on an inhomogeneous density distribution in a steady state.[28] Further modifications of the stochastic mPNP models need to be made for incorporating improvements in the deterministic mPNP models.

The aim of this paper

To summarize, the deterministic and stochastic mPNP models proposed so far are beneficial in the following respects: while the deterministic mPNP models have provided elaborate and

Open Access Article. Published on 26 May 2022. Downloaded on 7/19/2025 4:45:38 PM.
This article is licensed under a Creative Commons Attribution-NonCommercial 3.0 Unported Licence.

tractable methods to include short-range correlations and interactions of Coulombic and non-Coulombic origins, the stochastic mPNP models have demonstrated the relevance to correlation function analysis on fluctuation phenomena in uniform and steady states. Integration of the deterministic and stochastic mPNP models should lead to a deeper understanding of the electrokinetic phenomena in concentrated electrolytes. To pave the way for such an elaborate mPNP model, the stochastic mPNP models need to capture the benefits of the deterministic mPNP models.

Thus, this paper serves two purposes. The first aim is to provide a unified formulation that combines the above results of the deterministic and stochastic mPNP models. From the aspect of the deterministic mPNP models, we attempt, using the unified formulation, to add the stochastic term to the deterministic mPNP equations and to derive the semi-phenomenological modifications[5–10] from the first principle based on the liquid state theory. In terms of the stochastic mPNP models, on the other hand, the unified formulation justifies the inclusion of modified terms proposed by the deterministic mPNP models[5–10] into the stochastic equations.[13–15]

The second purpose is to determine when density and charge oscillations emerge in non-equilibrium steady states. To this end, we investigate stationary correlation functions which are averaged over the plane transverse to the applied electric field. The unified mPNP model yields the stationary correlation functions at equal times, which enables us to explore crossovers from monotonic to oscillatory decay of density–density and charge–charge correlations.

The organization of this paper

In what follows, we first present the summarized results on both the unified form of mPNP models (Section II) and the correlation function analysis to investigate steady states (Section III) before going into the details.

On the one hand, Table 1 in Section II summarizes the obtained forms compared to previous formulations. The essential achievement in terms of the theoretical formalism is clarified in Section IID. As detailed in Appendix A, the hybrid framework of the field-theoretic approach, the equilibrium[37,38] and dynamic[11] DFTs, and the liquid state theory justifies the modified Poisson equations[5–10,23,24,39–41] and the generalized Debye–Hückel equation for the self-energy.[10,25]

On the other hand, Fig. 2 in Section III provides a schematic summary of electric-field-dependent decay length prior to the equilibrium Kirkwood crossover in the external field direction. Fig. 2 illustrates not only the emergence of stripe states formed by segregation bands transverse to the applied field direction but also the intimate connection between the electric-field-induced shift of the decay length at the steady-sate Kirkwood crossover and the underscreening behaviors[19,20,29–31] observed in equilibrium electrolytes whose concentrations are higher than the conventional Kirkwood crossover point.[32–36] Section IIIE presents the 2D behaviors of oscillatory correlations above the Kirkwood crossover using heat maps, which corroborates the appearance of stripe states in the presence of relatively weak electric fields.

Section IV clarifies the detailed process to analytical and numerical results of the electric-field-induced Kirkwood crossover and the decay length using a couple of models typical for the liquid state theory. In Section V, we have discussions for comparing the theoretical predictions with experimental and simulation results.

II. Formulation results on modifications of PNP model

In the first place, this section summarizes the resulting formulation, according to Table 1 (Section IIA). As seen from the equation type given in the leftmost column of Table 1, we have verified two modifications of PNP equations using the SDFT of the symmetric primitive model specified in Section IIB. In Section IIC, we present fully modified PNP equations that incorporate into the PNP model density currents due to Gaussian noise fields as well as a self-energy contribution. Section IID describes the theoretical achievements in terms of the Dean–Kawasaki model.[11,26] In Section IIE, we investigate the linearized mPNP equations while neglecting the self-energy in order to obtain stationary correlation functions at equal times.

A. Comparison with previous theories

In Sections IIC and D, we will present the self-energy-modified PNP equations[10] and the linear mPNP equations.[13–15] Table 1 compares these equation sets with previous approaches.

Self-energy-modified PNP equations. Previous theories[5–12] have made two modifications. One is to improve the Poisson equation for the Coulomb interaction potential $\psi(\boldsymbol{r}, t)$ experienced by an ion (the higher-order Poisson eqn (15)).[5–10,21–24] The other is to make a self-energy correction to the Coulomb interaction term in the PNP equations (the self-energy term determined by the generalized Debye–Hückel eqn (21)),[10,25]

Table 1 Summary table of our formulation in comparison with previous theories on the mPNP models

Equation type		Modification of the Poisson equation	Self-energy contribution	Stochastic density current	Correlation functions
Self-energy-modified	Ref. 10	Eqn (15)[b]	Eqn (9), (20) and (21)	—	—
PNP equations	Ours	Eqn (14)[a] or (15)[b]	Eqn (9), (16) and (17)	Eqn (3) and (4)	TBD
Linear	Ref. 13–15	Poisson or eqn (14)[a]	—	Eqn (30)	Eqn (43)–(50)
mPNP equations	Ours	Eqn (14)[a]	—	Eqn (30)	Eqn (43)–(50)

[a] Finite-spread Poisson equation.[13,15,24,39–41] [b] Higher-order Poisson equation.[5–10,21–24]

 This journal is © The Royal Society of Chemistry 2022

Open Access Article. Published on 26 May 2022. Downloaded on 7/19/2025 4:45:38 PM.
This article is licensed under a Creative Commons Attribution-NonCommercial 3.0 Unported Licence.

thereby providing theoretical descriptions of ionic transport in agreement with simulation results; however, these modifications are empirical, and correlation functions have been beyond the scope due to the absence of stochastic current. Meanwhile, our self-energy-modified PNP equations, derived from the basic formulation of the SDFT (see Appendix A for details), verify the stochastic dynamics and encompass the above modifications.

Linear mPNP equations. Recently, the mPNP model covers the stochastic dynamics of density fluctuations around a uniform state while neglecting the self-energy contribution.[13,14] Furthermore, a finite-spread Poisson equation has been used in an *ad hoc* manner depending on a charge smearing model adopted.[15] The stochastic mPNP equations allow us to evaluate correlation functions, yielding either the ion concentration-dependent electrical conductivity or the long-range fluctuation-induced force.[14] In this study, we confirm the stochastic mPNP equations previously used as an approximation of the self-energy-modified PNP equations.[10] Accordingly, the use of the finite-spread Poisson equation[13,15,24,39–41] is validated from the decomposition of the direct correlation function (DCF) to extract the weight function $\omega(\boldsymbol{k})$, implying that we can improve the finite-spread Poisson equation systematically by adopting a more appropriate function form of $\omega(\boldsymbol{k})$ other than eqn (12).

B. Model

The 3D primitive model introduces three parameters, p, σ and ε, for concentrated electrolytes with a static electric field $\boldsymbol{E}$ applied: p-valent cations and anions are modeled by equisized charged hard spheres of diameter σ immersed in a structureless and uniform dielectric medium with dielectric constant ε at a temperature T. For later convenience, the external field $\boldsymbol{E}$ represents the conventional field multiplied by e/k_BT (see also the statement after eqn (A14)). Fig. 1 presents a schematic of the electric-field-driven primitive model in Cartesian coordinates where the external electric field $\boldsymbol{E}$ with its strength of $E = |\boldsymbol{E}|$ is parallel to the unit vector $\hat{\boldsymbol{e}}_x = (1,0,0)^T = \boldsymbol{E}/E$ in the direction of x-axis. There are two parallel plates in Fig. 1; however, the interplate distance is much larger than the sphere diameter, and we suppose that the finite size effect due to the presence of the plates is negligible.

The primitive model is characterized by a pairwise interaction potential $v_{lm}(\boldsymbol{r})$ between charged hard spheres with a separation distance of $r = |\boldsymbol{r}|$: $v_{11}(\boldsymbol{r})$, $v_{12}(\boldsymbol{r})$ and $v_{22}(\boldsymbol{r})$ represent cation-cation, cation-anion and anion-anion interactions, respectively. We have

$$v_{lm}(\boldsymbol{r}) = \begin{cases} \infty & (r < \sigma) \\ (-1)^{l+m} p^2 l_B / r & (r \geq \sigma), \end{cases} \tag{2}$$

where $l_B = e^2/(4\pi\varepsilon k_BT)$ denotes the Bjerrum length, the length at which the bare Coulomb interaction between two monovalent ions is exactly k_BT. It is noted that this paper defines all of the energetic quantities, including the pairwise interaction potentials, in units of k_BT.

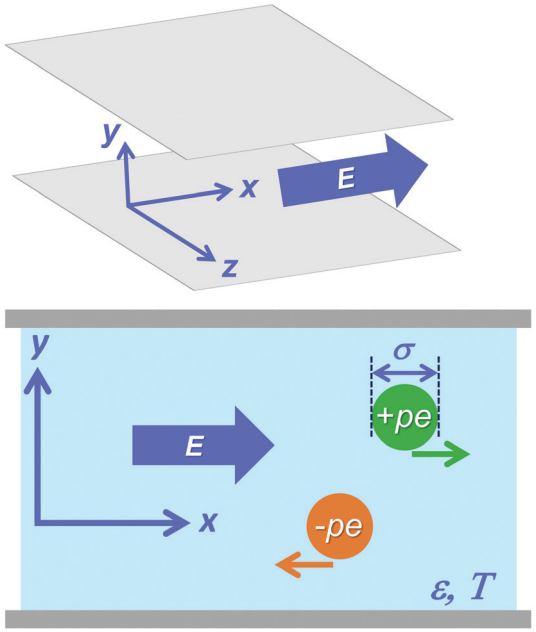

Fig. 1 A schematic of concentrated electrolytes under a static electric field $\boldsymbol{E}$ in Cartesian coordinates (top figure). The 3D primitive model is illustrated in the xy plane (lower figure). The definition of symbols is provided in the main text.

C. Self-energy-modified PNP equations: a full set of the resulting formulation

The conservation equation with stochastic current. In the conservation eqn (1) of the SDFT, the ionic current $\boldsymbol{J}_l(\boldsymbol{r}, t)$ consists of three parts:

$$\begin{aligned} \boldsymbol{J}_l(\boldsymbol{r}, t) &= (-1)^{l-1}\mathcal{D}n_l(\boldsymbol{r}, t)p\boldsymbol{E} - \mathcal{D}n_l(\boldsymbol{r}, t)\nabla\mu_l[\boldsymbol{n}] \\ &\quad - \sqrt{2\mathcal{D}n_l(\boldsymbol{r}, t)}\zeta(\boldsymbol{r}, t), \end{aligned} \tag{3}$$

where $\mathcal{D}$ and $\mu_l[\boldsymbol{n}]$ denote, respectively, the diffusion constant and the chemical potential as a functional of $\boldsymbol{n}(\boldsymbol{r}, t) = (n_1(\boldsymbol{r}, t), n_2(\boldsymbol{r}, t))^T$, and $\zeta(\boldsymbol{r}, t)$ represents an uncorrelated Gaussian noise field defined below. Incidentally, we have neglected an advection term,[15,16] $n_l(\boldsymbol{r}, t)\boldsymbol{u}(\boldsymbol{r}, t)$, on the right hand side (rhs) of eqn (3) with $\boldsymbol{u}(\boldsymbol{r}, t)$ denoting the solvent velocity field to satisfy the incompressibility condition $\nabla\cdot\boldsymbol{u} = 0$; this approximation is equivalent to supposing that $|\mathbf{u}| \ll |\mathcal{D}p\mathbf{E}|$.

Concrete forms of density current $\boldsymbol{J}_l(\boldsymbol{r}, t)$. The first term on the rhs of eqn (3) represents the reference current directly determined by $\boldsymbol{E}$. The chemical potential $\mu_l[\boldsymbol{n}]$ of the second term on the rhs of eqn (3) is given by

$$\mu_l[\boldsymbol{n}] = \ln n_l(\boldsymbol{r}, t) + U_l[\boldsymbol{n}], \tag{4}$$

using an instantaneous interaction energy $U_l[\boldsymbol{n}]$ per cation ($l = 1$) or anion ($l = 2$). Eqn (4) indicates that this part of the total current is due to contributions from ideal entropy and Coulomb interactions including steric effects. The last term on the rhs of eqn (3) corresponds to the stochastic current arising from $\zeta(\boldsymbol{r}, t)$ characterized by

$$\langle\zeta(\boldsymbol{r}, t)\zeta(\boldsymbol{r}', t')^T\rangle_\zeta = \delta(\boldsymbol{r} - \boldsymbol{r}')\delta(t - t'), \tag{5}$$

Open Access Article. Published on 26 May 2022. Downloaded on 7/19/2025 4:45:38 PM.
This article is licensed under a Creative Commons Attribution-NonCommercial 3.0 Unported Licence.

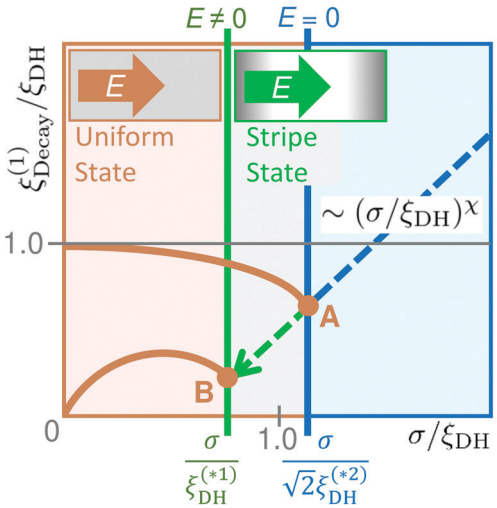

Fig. 2 A schematic summary of results obtained in this study is depicted in terms of the decay length $\xi^{(1)}_{\rm Decay}$ of either monotonic decay or damped oscillatory on a log–log plot of $\xi^{(1)}_{\rm Decay}/\xi_{\rm DH} = \bar{\kappa}\xi^{(1)}_{\rm Decay}$ *vs.* $\sigma/\xi_{\rm DH} = \bar{\kappa}\sigma$ where $\xi_{\rm DH} = \bar{\kappa}^{-1}$ denotes the smeared Debye–Hückel screening length defined by eqn (36). Our numerical results of $\xi^{(1)}_{\rm Decay}$ will be given in Fig. 3 and 8. In Fig. 2, these are shown using the solid brown lines terminated at nodes A and B, and the dashed green arrow from node A to node B, or from the Kirkwood crossover at $E = 0$ to that under electric field ($E \neq 0$). While the solid brown line terminated at node A ($E = 0$) converges to $\xi^{(1)}_{\rm Decay}/\xi_{\rm DH} = 1$ in the dilute limit, the solid brown line terminated at node B ($E \neq 0$) approaches zero in the dilute limit because of the finite decay length $\xi^{(1)}_{\rm Decay} = (pE)^{-1}$ (see also a discussion given at the end of Section IIIA). As illustrated by the upper inset, the green vertical line through node B marks $\sigma/\xi_{\rm DH} = \sigma/\xi^{(*1)}_{\rm DH}$, or the onset of shifted Kirkwood crossover from a uniform state to a stripe state without consideration of lane formation.[17,18] For comparison, we add the dashed blue line to show underscreening behavior in concentrated electrolytes without applied electric field beyond the conventional Kirkwood crossover indicated by the blue vertical line through node A; this blue line represents $\sigma/\xi_{\rm DH} = \sigma/(\sqrt{2}\xi^{(*2)}_{\rm DH})$, which is the conventional Kirkwood crossover value[32–36] in the range of 1.0 to 1.2 for symmetric electrolytes. Recent studies[20,29–31] have demonstrated that $\xi^{(1)}_{\rm Decay}/\xi_{\rm DH} \sim (\sigma/\xi_{\rm DH})^{\chi}$ with the exponent of $\chi > 1$ in a damped oscillatory state. It will be seen from Fig. 3(b) and 8(b) that a similar scaling relation holds for the dashed green arrow.

with the subscript "ζ" representing the Gaussian noise averaging in space and time.

Following the mPNP equations proposed so far,[5–10,13–16] $U_l[\boldsymbol{n}]$ is further divided into two parts:

$$U_l[\boldsymbol{n}] = (-1)^{l-1}\psi(\boldsymbol{r}, t) + \frac{u(\boldsymbol{r}, t)}{2}, \tag{6}$$

where $(-1)^{l-1}\psi(\boldsymbol{r}, t)$ and $u(\boldsymbol{r}, t)/2$ denote, respectively, the instantaneous interaction potential and the instantaneous self-energy per ion. We define $\psi(\boldsymbol{r}, t)$ by

$$\psi(\boldsymbol{r}, t) = -\int \mathrm{d}^3\boldsymbol{r}' c(\mathbf{r} - \boldsymbol{r}')q(\boldsymbol{r}', t), \tag{7}$$

using the DCF $c(\boldsymbol{r} - \boldsymbol{r}')$ and an instantaneous charge density,

$$peq(\boldsymbol{r}, t) = pe\{n_1(\boldsymbol{r}, t) - n_2(\boldsymbol{r}, t)\}. \tag{8}$$

By definition of the DCF, the potential function $\psi(\boldsymbol{r}, t)$ defined in eqn (7) corresponds to the conventional Coulomb potential multiplied by $pe/k_{\rm B}T$ (see also eqn (13)). It follows that $q(\boldsymbol{r}, t)$ in eqn (7) is not an instantaneous charge density but is merely the concentration difference ($q = n_1 - n_2$) as seen from eqn (8).

Meanwhile, our resulting formulation provides the self-energy as follows:

$$\frac{u(\boldsymbol{r}, t)}{2} = \frac{p^2}{2}\lim_{\boldsymbol{r}' \to \boldsymbol{r}}\{G(\boldsymbol{r} - \boldsymbol{r}') - G_0(\boldsymbol{r} - \boldsymbol{r}')\}, \tag{9}$$

where bare and dressed propagators, $G_0(\boldsymbol{r} - \boldsymbol{r}')$ and $G(\boldsymbol{r} - \boldsymbol{r}')$, are given by

$$p^2G_0(\boldsymbol{r} - \boldsymbol{r}') = -c(\boldsymbol{r} - \boldsymbol{r}'), \tag{10}$$

$$p^2G(\boldsymbol{r} - \boldsymbol{r}') = -h(\boldsymbol{r} - \boldsymbol{r}'), \tag{11}$$

with $h(\boldsymbol{r} - \boldsymbol{r}')$ denoting the total correlation function between ions of the same kind.

We investigate the following model forms as the DCFs:

$$\omega(\boldsymbol{k}) = \begin{cases} \mathrm{e}^{-(k\sigma)^2/2} \\ \cos(k\sigma), \end{cases} \tag{12}$$

in the Fourier transform of the DCF given by

$$-c(\boldsymbol{k}) = \frac{4\pi p^2 l_{\rm B}}{\boldsymbol{k}^2}\omega(-\boldsymbol{k}), \tag{13}$$

where $|\boldsymbol{k}| = k$. While the former expression of $\omega(\boldsymbol{k})$ in eqn (12) represents the Gaussian charge smearing model[35,40] and has been used in the hypernetted chain approximation of one-component ionic fluids,[42] the latter form in eqn (12) indicates the restriction of Coulomb interactions to the separation of $|\boldsymbol{r} - \boldsymbol{r}'| > \sigma$ with a cutoff at $|\boldsymbol{r} - \boldsymbol{r}'| = \sigma$ and is an approximate form of the modified MSA model[43] as shown in Appendix A2.

Finite-spread or higher-order Poisson equation. Combining eqn (7), (12) and (13), we have

$$-\nabla^2\psi(\boldsymbol{r} - \boldsymbol{r}') = 4\pi p^2 l_{\rm B}\int \mathrm{d}^3\boldsymbol{r}'\omega(\boldsymbol{r} - \boldsymbol{r}')q(\boldsymbol{r}', t), \tag{14}$$

which will be referred to as the finite-spread Poisson equation after the finite-spread Poisson–Boltzmann equation; both equations consider the charge distribution inside a charged sphere using a weight function $\omega(\boldsymbol{r} - \boldsymbol{r}')$. As shown in Appendix A2, eqn (14) transforms to

$$k_{\rm B}T\varepsilon\left(\frac{\sigma^2}{2}\nabla^2 - 1\right)\nabla^2\psi(\boldsymbol{r} - \boldsymbol{r}') = (pe)^2q(\boldsymbol{r}, t), \tag{15}$$

when performing the low wavenumber expansion of $\omega(\boldsymbol{k})$, similarly to the transformation from the finite-spread Poisson–Boltzmann equation to the higher-order one for one-component fluids.[24] Eqn (15) will be referred to as the higher-order Poisson equation[5–10,21–24] for comparison with the finite-spread Poisson eqn (14), though often called either the Poisson-Fermi equation or the Bazant–Storey–Kornyshev equation.[21]

A generalized Debye–Hückel equation. It follows from eqn (10)–(13) that the DCF and the total correlation function, $c(\boldsymbol{r} - \boldsymbol{r}')$ and $h(\boldsymbol{r} - \boldsymbol{r}')$, obey a modified Poisson equation and a generalized Debye–Hückel equation, respectively: we have

$$-\nabla^2G_0(\boldsymbol{r} - \boldsymbol{r}') = 4\pi l_{\rm B}\omega(\boldsymbol{r} - \boldsymbol{r}'), \tag{16}$$

This journal is © The Royal Society of Chemistry 2022

Open Access Article. Published on 26 May 2022. Downloaded on 7/19/2025 4:45:38 PM. This article is licensed under a Creative Commons Attribution-NonCommercial 3.0 Unported Licence.

whereas the Orstein–Zernike equation reads

$$-\nabla^2 G(\boldsymbol{r}-\boldsymbol{r}') + \int \mathrm{d}^3\boldsymbol{r}''\omega(\boldsymbol{r}-\boldsymbol{r}'')\kappa^2(\boldsymbol{r}'')G(\boldsymbol{r}''-\boldsymbol{r}') = 4\pi l_{\mathrm{B}}\omega(\boldsymbol{r}-\boldsymbol{r}'), \tag{17}$$

where a generalized Debye–Hückel length $\kappa^{-1}(\boldsymbol{r})$ has been defined as

$$\kappa^{-1}(\boldsymbol{r}) = \{4\pi l_{\mathrm{B}} p^2 \rho(\boldsymbol{r}, t)\}^{-1/2}, \tag{18}$$

$$\rho(\boldsymbol{r}, t) = n_1(\boldsymbol{r}, t) + n_2(\boldsymbol{r}, t). \tag{19}$$

Eqn (16) and (17) for point charges (σ = 0) reduce, respectively, to

$$-\nabla^2 G_0(\boldsymbol{r}-\boldsymbol{r}') = 4\pi l_{\mathrm{B}}\delta(\boldsymbol{r}-\boldsymbol{r}') \tag{20}$$

and

$$-\nabla^2 G(\boldsymbol{r}-\boldsymbol{r}') + \kappa^2(\boldsymbol{r})G(\boldsymbol{r}-\boldsymbol{r}') = 4\pi l_{\mathrm{B}}\delta(\boldsymbol{r}-\boldsymbol{r}') \tag{21}$$

because of

$$\lim_{\sigma\to 0}\omega(\boldsymbol{r}-\boldsymbol{r}') = \delta(\boldsymbol{r}-\boldsymbol{r}'), \tag{22}$$

as confirmed from eqn (12). Eqn (21) corresponds to the generalized Debye–Hückel equation previously used.[10,25]

D. Theoretical achievement in terms of the Dean–Kawasaki model

In Appendices A and B, we prove that the Dean–Kawasaki model can be approximated by the formula given by eqn (3)–(11) for concentrated electrolytes: the hybrid framework of the equilibrium DFT and field-theoretic treatment transforms the original Dean–Kawasaki equation[11,26] to a tractable expression for binary ionic fluids without *ad hoc* modifications. Here we clarify the theoretical achievement instead of going into the detailed formulations presented in Appendix A. It is found from eqn (A2), (B1), (B2) and (B3) that the straightforward use of the original DK model provides exactly

$$U_l[\boldsymbol{n}] = (-1)^{l-1}\psi_0(\boldsymbol{r}, t) - \frac{v_{ll}(0)}{2}, \tag{23}$$

$$\psi_0(\boldsymbol{r}, t) = \int \mathrm{d}^3\boldsymbol{r}' v_{ll}(\boldsymbol{r}-\boldsymbol{r}')q(\boldsymbol{r}', t). \tag{24}$$

It follows from eqn (3), (6) and (23) that the electrostatic contribution to ionic current reads

$$-\mathcal{D}\boldsymbol{n}_l(\boldsymbol{r}, t)\nabla U_l[\boldsymbol{n}] = \mathcal{D}\boldsymbol{n}_l(\boldsymbol{r}, t)\left\{(-1)^{l-1}\nabla\psi(\boldsymbol{r}, t) + \frac{\nabla u(\boldsymbol{r}, t)}{2}\right\} \tag{25}$$

$$= \mathcal{D}\boldsymbol{n}_l(\boldsymbol{r}, t)\{(-1)^{l-1}\nabla\psi_0(\boldsymbol{r}, t)\} \tag{26}$$

because of $\nabla v_{ll}(0)$ = 0. Comparison between eqn (25) and (26) reveals that the SDFT based on the above hybrid framework justifies

$$|\nabla\{\psi_0(\boldsymbol{r}, t) - \psi(\boldsymbol{r}, t)\}| \approx \left|\frac{\nabla c(0, t)}{2}\right| \tag{27}$$

in the Gaussian approximation of the auxiliary potential field (see Appendix A for details), where use has been made of the relation, $\nabla u(\boldsymbol{r}) = \nabla \lim_{\boldsymbol{r}'\to\boldsymbol{r}} c(\boldsymbol{r}-\boldsymbol{r}', t) \equiv \nabla c(0, t)$. Our achievement in terms of the theoretical formalism is essentially to validate eqn (27).

E. Linear mPNP equations and the associated correlation functions

The matrix representation. Let us introduce two vectors, $\boldsymbol{\theta}(\boldsymbol{r}, t)$ and $\boldsymbol{\eta}(\boldsymbol{r}, t)$, for having a compact form of the mPNP equation set:

$$\boldsymbol{\theta}(\boldsymbol{r}, t) = \begin{pmatrix}\rho(\boldsymbol{r}, t)\\ q(\boldsymbol{r}, t)\end{pmatrix}, \tag{28}$$

$$\boldsymbol{\eta}(\boldsymbol{r}, t) = \begin{pmatrix}\nabla\cdot\zeta(\boldsymbol{r}, t)\\ \nabla\cdot\zeta'(\boldsymbol{r}, t)\end{pmatrix}, \tag{29}$$

where $\rho(\boldsymbol{r}, t)$ and $q(\boldsymbol{r}, t)$ have been defined in eqn (19) and (8), respectively, and $\zeta'(\boldsymbol{r}, t)$ satisfies the relation (5) as well as $\zeta(\boldsymbol{r}, t)$. We perform the change of variables from $\boldsymbol{n}(\boldsymbol{r}, t)$ to $\boldsymbol{q}(\boldsymbol{r}, t)$ in the linearization of the mPNP equation set given by eqn (1) and eqn (3)–(6) with the self-energy term (9) being dropped. Thus, we obtain the stochastic currents, $\boldsymbol{J}_\rho$ and $\boldsymbol{J}_q$, from linearizing the current given by eqn (3) (see Appendix A for details):

$$\begin{aligned}\begin{pmatrix}\boldsymbol{J}_\rho(\boldsymbol{r}, t)\\ \boldsymbol{J}_q(\boldsymbol{r}, t)\end{pmatrix} &= \begin{pmatrix}\boldsymbol{J}_1(\boldsymbol{r}, t) + \boldsymbol{J}_2(\boldsymbol{r}, t)\\ \boldsymbol{J}_1(\boldsymbol{r}, t) - \boldsymbol{J}_2(\boldsymbol{r}, t)\end{pmatrix}\\ &= -\mathcal{D}\begin{pmatrix}\nabla\rho(\boldsymbol{r}, t) - q(\boldsymbol{r}, t)p\boldsymbol{E}\\ \nabla q(\boldsymbol{r}, t) + 2\bar{n}\nabla\psi(\boldsymbol{r}, t) - \rho(\boldsymbol{r}, t)p\boldsymbol{E}\end{pmatrix}\\ &\quad - \sqrt{4\mathcal{D}\bar{n}}\begin{pmatrix}\zeta(\boldsymbol{r}, t)\\ \zeta'(\boldsymbol{r}, t)\end{pmatrix},\end{aligned} \tag{30}$$

using the smeared density $\bar{n}$ of cations or anions. We insert the expression (30) into the conservation equation for $\rho(\boldsymbol{r}, t)$ and $q(\boldsymbol{r}, t)$:

$$\partial_t\boldsymbol{\theta}(\boldsymbol{r}, t) = -\nabla\cdot\begin{pmatrix}\boldsymbol{J}_\rho(\boldsymbol{r}, t)\\ \boldsymbol{J}_q(\boldsymbol{r}, t)\end{pmatrix}, \tag{31}$$

which is Fourier transformed to

$$\partial_t\boldsymbol{\theta}(\boldsymbol{k}) = -\mathcal{D}\mathcal{K}(\boldsymbol{k})\boldsymbol{\theta}(-\boldsymbol{k}, t) + \sqrt{4\mathcal{D}\bar{n}}\boldsymbol{\eta}(\boldsymbol{k}). \tag{32}$$

In eqn (14), the matrix to determine restoring forces is expressed as

$$\mathcal{K}(\boldsymbol{k}) = \begin{pmatrix}\boldsymbol{k}^2 & ik_x pE\\ ik_x pE & \mathcal{G}_1(\boldsymbol{k})\end{pmatrix}, \tag{33}$$

$$\mathcal{G}_1(\boldsymbol{k}) = \boldsymbol{k}^2 + \bar{\kappa}^2\omega(\boldsymbol{k}), \tag{34}$$

noting that the finite-spread Poisson eqn (14) yields

$$-2\bar{n}\boldsymbol{k}^2\psi(\boldsymbol{k}) = -8\pi p^2 l_{\mathrm{B}}\bar{n}\omega(\boldsymbol{k})q(-\boldsymbol{k}) = -\bar{\kappa}^2\omega(\boldsymbol{k})q(-\boldsymbol{k}), \tag{35}$$

Open Access Article. Published on 26 May 2022. Downloaded on 7/19/2025 4:45:38 PM.
This article is licensed under a Creative Commons Attribution-NonCommercial 3.0 Unported Licence.

where we have defined the smeared Debye–Hückel length,

$$\xi_{\mathrm{DH}} = \bar{\kappa}^{-1} \equiv (8\pi p^2 l_{\mathrm{B}} \bar{n})^{-1/2}, \tag{36}$$

other than $\kappa^{-1}(\boldsymbol{r}, t)$ defined by eqn (18). In eqn (33), the anisotropy of the $\boldsymbol{k}$-space is associated with the direction of applied electric field (*i.e.*, $\hat{\boldsymbol{e}}_x = \boldsymbol{E}/E$) and we have

$$k_x = \boldsymbol{k}\cdot\hat{\boldsymbol{e}}_x, \tag{37}$$

or

$$\boldsymbol{k} = k_x\hat{\boldsymbol{e}}_x + \boldsymbol{k}_\perp, \tag{38}$$

$$\boldsymbol{k}_\perp = (0, k_y, k_z)^T. \tag{39}$$

Density–density and charge–charge correlation functions. One of the benefits of stochastic equations is that correlation functions are calculated straightforwardly. Here we consider density–density and charge–charge correlation functions at equal times, which are defined using the equal-time correlation matrix as follows:

$$\begin{aligned}\mathcal{C}(\boldsymbol{k}, t) &= \left\langle \boldsymbol{\theta}(\boldsymbol{k}, t)\boldsymbol{\theta}(-\boldsymbol{k}, t)^{\mathrm{T}} \right\rangle_\zeta \\ &= \begin{pmatrix} \langle \rho(\boldsymbol{k}, t)\rho(-\boldsymbol{k}, t)\rangle_\zeta & \langle q(\boldsymbol{k}, t)\rho(-\boldsymbol{k}, t)\rangle_\zeta \\ \langle \rho(\boldsymbol{k}, t)q(-\boldsymbol{k}, t)\rangle_\zeta & \langle q(\boldsymbol{k}, t)q(-\boldsymbol{k}, t)\rangle_\zeta \end{pmatrix} \\ &= \begin{pmatrix} \mathcal{C}_{\rho\rho}(\boldsymbol{k}, t) & \mathcal{C}_{q\rho}(\boldsymbol{k}, t) \\ \mathcal{C}_{\rho q}(\boldsymbol{k}, t) & \mathcal{C}_{qq}(\boldsymbol{k}, t) \end{pmatrix}. \end{aligned} \tag{40}$$

In the matrix elements given by eqn (40), $\mathcal{C}_{\rho\rho}$ and $\mathcal{C}_{qq}$ are the target correlation functions. To be precise, $p^2e^2\mathcal{C}_{qq}(\boldsymbol{k}, t)$ is the charge–charge correlation function, according to the definition of eqn (8). For brevity, however, we will refer to $\mathcal{C}_{qq}(\boldsymbol{k}, t)$ as the charge–charge correlation function.

We focus on the steady-state solutions of the correlation functions:

$$\mathcal{C}^{\mathrm{st}}_{\rho\rho}(\boldsymbol{k}) = \lim_{t\to\infty} \mathcal{C}_{\rho\rho}(\boldsymbol{k}, t), \tag{41}$$

$$\mathcal{C}^{\mathrm{st}}_{qq}(\boldsymbol{k}) = \lim_{t\to\infty} \mathcal{C}_{qq}(\boldsymbol{k}, t). \tag{42}$$

As detailed below, these are written as

$$\frac{1}{(2\pi)^3}\begin{pmatrix} \mathcal{C}^{\mathrm{st}}_{\rho\rho}(\boldsymbol{k}) \\ \mathcal{C}^{\mathrm{st}}_{qq}(\boldsymbol{k}) \end{pmatrix} = \frac{2\bar{n}\mathcal{G}_2(\boldsymbol{k})}{\det\mathcal{P}(\boldsymbol{k})}\widetilde{\mathcal{P}}(\boldsymbol{k})\begin{pmatrix} \boldsymbol{k}^2 \\ \boldsymbol{k}^2 \end{pmatrix}, \tag{43}$$

where we have

$$\frac{\mathcal{G}_2(\boldsymbol{k})}{\det\mathcal{P}} = \frac{1}{\mathcal{G}_2(\boldsymbol{k})\{\boldsymbol{k}^2\mathcal{G}_1(\boldsymbol{k}) + k_x^2(pE)^2\}}, \tag{44}$$

$$\mathcal{G}_2(\boldsymbol{k}) = 2\boldsymbol{k}^2 + \bar{\kappa}^2\omega(\boldsymbol{k}), \tag{45}$$

and the adjugate matrix of $\mathcal{P}(\boldsymbol{k})$, signified by $\widetilde{\mathcal{P}}(\boldsymbol{k})$, reads

$$\widetilde{\mathcal{P}}(\boldsymbol{k}) = \begin{pmatrix} \mathcal{G}_1(\boldsymbol{k})\mathcal{G}_2(\boldsymbol{k}) + k_x^2(pE)^2 & k_x^2(pE)^2 \\ k_x^2(pE)^2 & \boldsymbol{k}^2\mathcal{G}_2(\boldsymbol{k}) + k_x^2(pE)^2 \end{pmatrix}. \tag{46}$$

Eqn (44) indicates that both $\mathcal{C}^{\mathrm{st}}_{\rho\rho}$ and $\mathcal{C}^{\mathrm{st}}_{qq}$ have identical poles under the external electric field $\boldsymbol{E}$.

In the limit of $k \to 0$, we have

$$\frac{1}{(2\pi)^3}\begin{pmatrix} \mathcal{C}^{\mathrm{st}}_{\rho\rho}(0) \\ \mathcal{C}^{\mathrm{st}}_{qq}(0) \end{pmatrix} = \begin{pmatrix} 2\bar{n} \\ 0 \end{pmatrix}. \tag{47}$$

Then, we divide $\mathcal{C}^{\mathrm{st}}_{\rho\rho}(\boldsymbol{k})$ into two parts: $\mathcal{C}^{\mathrm{st}}_{\rho\rho}(\boldsymbol{k})/(2\pi)^3 = 2\bar{n} + \Delta\mathcal{C}^{\mathrm{st}}_{\rho\rho}(\boldsymbol{k})/(2\pi)^3$ where

$$\frac{1}{(2\pi)^3}\Delta\mathcal{C}^{\mathrm{st}}_{\rho\rho}(\boldsymbol{k}) = \frac{-\bar{\kappa}^2\omega(\boldsymbol{k})k_x^2(pE)^2}{\mathcal{G}_2(\boldsymbol{k})\{\boldsymbol{k}^2\mathcal{G}_1(\boldsymbol{k}) + k_x^2(pE)^2\}} \tag{48}$$

is directly related to total correlation functions, or essential parts of density–density correlations.

In the limit of $\sigma \to 0$, on the other hand, we have $\omega(\boldsymbol{k}) = 1$ and eqn (43) is approximated by

$$\frac{1}{(2\pi)^3}\begin{pmatrix} \mathcal{C}^{\mathrm{st}}_{\rho\rho}(\boldsymbol{k}) \\ \mathcal{C}^{\mathrm{st}}_{qq}(\boldsymbol{k}) \end{pmatrix} = 2\bar{n}\left\{\begin{pmatrix} 1 \\ 1 \end{pmatrix} + \frac{k_x^2(pE\bar{\kappa}^{-1})^2}{\boldsymbol{k}^2 + k_x^2(pE\bar{\kappa}^{-1})^2}\begin{pmatrix} -1 \\ 1 \end{pmatrix}\right\}\begin{pmatrix} 1 \\ \boldsymbol{k}^2/\bar{\kappa}^2 \end{pmatrix} \tag{49}$$

in the low wavenumber region of $k_x\bar{\kappa}^{-1} \ll 1$ (see Appendix D for the derivation). It should be noted that eqn (49) agrees with the expression previously obtained in a different manner[14] and that the Fourier transform of eqn (49) has been demonstrated to provide anisotropic long-range correlation functions exhibiting a power-law behavior with a dipolar character.[14] At low field strength of $pE\bar{\kappa}^{-1} \ll 1$, eqn (49) converges to

$$\frac{1}{(2\pi)^3}\begin{pmatrix} \mathcal{C}^{\mathrm{st}}_{\rho\rho}(\boldsymbol{k}) \\ \mathcal{C}^{\mathrm{st}}_{qq}(\boldsymbol{k}) \end{pmatrix} \to 2\bar{n}\begin{pmatrix} 1 \\ \boldsymbol{k}^2/\bar{\kappa}^2 \end{pmatrix}, \tag{50}$$

clarifying that low electric-field-driven electrolytes in steady states mimic weakly interacting ionic fluids without applied electric field on a large scale and that $\mathcal{C}^{\mathrm{st}}_{qq}(\boldsymbol{k})$ given by eqn (50) satisfies not only the electroneutrality but also the Stillinger–Lovett second-moment condition.

III. Correlation function analysis: electric-field-induced crossover to a damped oscillatory state

The first two subsections will be devoted to what is implied by the complicated forms (43)–(48) of correlation functions, $\mathcal{C}^{\mathrm{st}}_{qq}(\boldsymbol{k})$ and $\Delta\mathcal{C}^{\mathrm{st}}_{\rho\rho}(\boldsymbol{k})$, especially focusing on the high wavenumber in the external field direction. While Section IIIA provides the pole equations of the correlation functions, Section IIIB clarifies the electric-field-induced oscillations when considering the solutions to the pole eqn (66), or an anisotropic crossover from monotonic to oscillatory decay of correlations along the direction of applied electric field. Before going into the numerical details of the results obtained from the pole eqn (66), Section IIIC aims to understand the relationship between the Kirkwood crossover at $E = 0$ and $E \neq 0$ using Fig. 2, a schematic plot of the decay length $\xi^{(1)}_{\mathrm{Decay}}$. After presenting the schematic summary, Section IIID explains how the crossover point is determined in the anisotropic

 This journal is © The Royal Society of Chemistry 2022

Open Access Article. Published on 26 May 2022. Downloaded on 7/19/2025 4:45:38 PM.
This article is licensed under a Creative Commons Attribution-NonCommercial 3.0 Unported Licence.

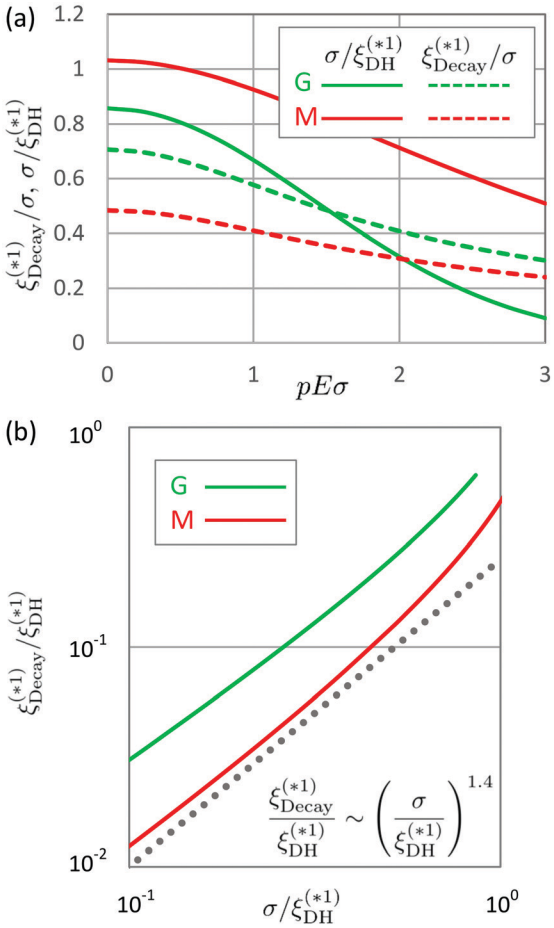

Fig. 3 Comparison between the electric-field-dependent length results which are obtained from the Gaussian charge smearing model (abbreviated as "G" and represented by green lines) and the modified MSA model (abbreviated as "M" and represented by red lines). Section IVB presents the detailed formulation to obtain the results given in this figure. (a) The electric-field dependencies of the Debye–Hückel length $\xi_{DH}^{(*1)} = 1/\bar{\kappa}^{(*1)}$ and the decay length $\xi_{Decay}^{(*1)}$ at the Kirkwood crossover are shown by the plot of $\sigma/\xi_{DH}^{(*1)}$ and $\xi_{Decay}^{(*1)}/\sigma$ against $pE\sigma$, an energetic measure of electric field strength in units of k_BT. While the solid lines represent $\sigma/\xi_{DH}^{(*1)}$, the dashed lines $\xi_{Decay}^{(*1)}/\sigma$. The related equations are as follows: green solid line (eqn (99)); green dashed line (eqn (102)); red solid and dashed lines (eqn (105) and (106)). (b) A log–log plot of $\sigma/\xi_{DH}^{(*1)}$-dependencies of $\xi_{Decay}^{(*1)}/\xi_{DH}^{(*1)}$. The dotted line, as a guide to the eye, indicates a scaling relation $\xi_{Decay}^{(*1)}/\xi_{DH}^{(*1)} \sim (\sigma/\xi_{DH}^{(*1)})^{1.4}$.

approximation of the pole eqn (66). In the anisotropic approximation (53), we can analytically investigate the electric-field-induced Kirkwood crossover (see Section IV for details). Fig. 3 in Section IIID gives the numerical results on the E-dependencies of both the decay length $\xi_{Decay}^{(*1)}$ and the smeared Debye–Hückel length $\xi_{DH}^{(*1)}$ at the Kirkwood crossover points. Last, Section IIIE presents various results on the 2D inverse Fourier transforms of $\Delta C_{\rho\rho}^{st}(\boldsymbol{k})$. We will see anisotropic density–density correlations reflecting the emergence of stripe states in a high-density region above the Kirkwood crossover.

A. Electric-field-induced synchronization between the emergences of density and charge oscillations

It is found from the denominator on the rhs of eqn (44) that the obtained correlation functions given by eqn (43)–(48) provide the following pole equations:

$$\left(\boldsymbol{k}^{(1)}\right)^2 + \bar{\kappa}^2\omega(\boldsymbol{k}^{(1)}) + \frac{\left(k_x^{(1)}\right)^2}{\left(\boldsymbol{k}^{(1)}\right)^2}(pE)^2 = 0, \tag{51}$$

$$2(\boldsymbol{k}^{(2)})^2 + \bar{\kappa}^2\omega(\boldsymbol{k}^{(2)}) = 0, \tag{52}$$

which remarkably apply to both density–density and charge–charge correlation functions. Namely, both density–density and charge–charge correlation functions exhibit the same behavior.

Let us discuss the concrete behaviors particularly in the anisotropic approximation of eqn (39) such that

$$\boldsymbol{k}^{(j)} \approx k_x^{(j)}\hat{\boldsymbol{e}}_x \tag{53}$$

(see Section IIIB for details). Focusing on the onset of oscillatory decay of correlations (or the Kirkwood crossover) at a fixed electric field, a summary provided in advance is threefold:

1. Simultaneous emergence of density and charge oscillations. The weight function $\omega(\boldsymbol{k})$ multiplied by $\bar{\kappa}^2$ allows us to have complex solutions to the pole eqn (51) and (52), other than purely imaginary solutions. The appearance of real solutions corresponds to the onset of oscillatory correlations. Hence, we find that eqn (51) and (52), which are equally valid for density–density and charge–charge correlations, lead to simultaneous emergence of density and charge oscillations. It is striking that the correlation function analysis directly predicts the electric-field-induced synchronization between the emergences of density and charge oscillations. The simultaneous occurrence of crossovers is in contrast to equilibrium crossover phenomena which emerge separately: the equilibrium density–density and charge–charge correlation functions exhibit the Fisher–Widom[31,36,44] and Kirkwood[31–36] crossovers, respectively.

2. Shifted crossover from monotonic to oscillatory decay of correlations. We consider the case where a smallest value of the purely imaginary solution to either eqn (51) or (52) exists for

$$\bar{\kappa}\sigma \le \bar{\kappa}^{(*j)}\sigma, \tag{54}$$

with the superscripts, (*1) and (*2), of the maxima denoting the upper bounds for eqn (51) and (52), respectively. Namely, the solutions to eqn (51) and (52) become complex beyond $\bar{\kappa}^{(*1)}\sigma$ and $\bar{\kappa}^{(*2)}\sigma$, respectively. It can be readily seen from eqn (52) that $\bar{\kappa}^{(*2)}\sigma$ is independent of E but is larger than the conventional Kirkwood crossover value[32–36] in the range of $1.0 < \bar{\kappa}^*\sigma < 1.2$ for symmetric electrolytes in equilibrium where the pole equation is $\boldsymbol{k}^2 + (\bar{\kappa}^*)^2\omega(\boldsymbol{k}) = 0$: it follows from eqn (52) that

$$\bar{\kappa}^*\sigma = \frac{\bar{\kappa}^{(*2)}\sigma}{\sqrt{2}} = \frac{\sigma}{\sqrt{2}\xi_{DH}^{(*2)}}. \tag{55}$$

In contrast, eqn (51) implies that $\bar{\kappa}^{(*1)}\sigma$ depends on E and is smaller than the above Kirkwood crossover value at $E = 0$ due to additional screening effect measured by pE.

Open Access Article. Published on 26 May 2022. Downloaded on 7/19/2025 4:45:38 PM.
This article is licensed under a Creative Commons Attribution-NonCommercial 3.0 Unported Licence.

3. Finite decay length in the dilute limit. Eqn (51) and (52) are reduced to

$$f_1(k_x^{(1)}) \equiv (k_x^{(1)})^2 + \bar{\kappa}^2 + (pE)^2 = 0, \tag{56}$$

$$f_2(k_x^{(2)}) \equiv (k_x^{(2)})^2 + 0.5\bar{\kappa}^2 = 0, \tag{57}$$

respectively, when considering the anisotropic approximation (53) and $\omega(\boldsymbol{k}) = 1$ for simplicity. In the dilute limit of $\bar{\kappa} \to 0$, eqn (56) yields a finite decay length $\xi_{\mathrm{Decay}}^{(1)} \approx (pE)^{-1}$ (see Section IIIB for detailed derivation), whereas eqn (57) ensures the divergent behavior of the decay length $\xi_{\mathrm{Decay}}^{(2)}$ given by $\xi_{\mathrm{Decay}}^{(2)} = \sqrt{2}\bar{\kappa}^{-1}$.

The non-vanishing decay length $\xi_{\mathrm{Decay}}^{(1)} \approx (pE)^{-1}$ helps us to understand the physics of the decay mode on target. We explain below the decay length $\xi_{\mathrm{Decay}}^{(1)} \approx (pE)^{-1}$ in terms of competing electrokinetics between electrophoresis and free diffusion. We have an electrophoresis time, $L/(\mathcal{D}pE)$, for a variable length L because the electrophoretic velocity is given by $(\mathcal{D}/k_{\mathrm{B}}T)pEk_{\mathrm{B}}T = \mathcal{D}pE$, remembering that the force pE exerted on a single ion by the applied electric field is defined in units of $k_{\mathrm{B}}T$ and that the mobility is given by $\mathcal{D}/k_{\mathrm{B}}T$ according to the Einstein relation. It follows that the equality between a required time for electrophoresis and free diffusion reads

$$\frac{L}{\mathcal{D}pE} = \frac{L^2}{\mathcal{D}}, \tag{58}$$

which is equivalent to the above relation $\xi_{\mathrm{Decay}}^{(1)} \approx (pE)^{-1}$ when $L = \xi_{\mathrm{Decay}}^{(1)}$.

Hence, eqn (58) implies that $\xi_{\mathrm{Decay}}^{(1)} \approx (pE)^{-1}$ is related to an electrokinetic crossover length. In the smaller scale of $L < \xi_{\mathrm{Decay}}^{(1)}$, free diffusion is dominant, and the electrophoretic migration path is blurred by diffusion. Meanwhile, for an electrophoresis dominant length scale $L > \xi_{\mathrm{Decay}}^{(1)}$, fluctuations in diffusion processes become negligible in comparison with electrophoretic migration: spatial distribution of charged spheres in a steady state is mainly determined by particles migrating uniformly. This electrokinetic aspect of a steady state provides an explanation of the decay length $\xi_{\mathrm{Decay}}^{(1)} \approx (pE)^{-1}$ that remains finite even in the dilute limit of $\bar{\kappa} \to 0$.

B. Electric-field-induced Kirkwood crossover

Let $\boldsymbol{r}_\perp$ be a transverse vector $\boldsymbol{r}_\perp = (0, y, z)^{\mathrm{T}}$ similar to $\boldsymbol{k}_\perp$ defined by eqn (39) (see also Fig. 1). The Fourier transform then reads

$$\Delta\mathcal{C}_{\rho\rho}^{\mathrm{st}}(\boldsymbol{k}) = \int \mathrm{d}^2\boldsymbol{r}_\perp \int \mathrm{d}x \Delta\mathcal{C}_{\rho\rho}^{\mathrm{st}}(\boldsymbol{r}) \mathrm{e}^{-ik_x x - i\boldsymbol{k}_\perp\cdot\boldsymbol{r}_\perp}, \tag{59}$$

$$\mathcal{C}_{qq}^{\mathrm{st}}(\boldsymbol{k}) = \int \mathrm{d}^2\boldsymbol{r}_\perp \int \mathrm{d}x \mathcal{C}_{qq}^{\mathrm{st}}(\boldsymbol{r}) \mathrm{e}^{-ik_x x - i\boldsymbol{k}_\perp\cdot\boldsymbol{r}_\perp}. \tag{60}$$

We consider the real-space representations of $\Delta\mathcal{C}_{\rho\rho}^{\mathrm{st}}(k_x)$ and $\mathcal{C}_{qq}^{\mathrm{st}}(k_x)$ defined by

$$\frac{1}{2\pi}\begin{pmatrix} \Delta\mathcal{C}_{\rho\rho}^{\mathrm{st}}(k_x) \\ \mathcal{C}_{qq}^{\mathrm{st}}(k_x) \end{pmatrix} = \frac{1}{(2\pi)^3}\int \mathrm{d}^2\boldsymbol{k}_\perp \begin{pmatrix} \Delta\mathcal{C}_{\rho\rho}^{\mathrm{st}}(\boldsymbol{k}) \\ \mathcal{C}_{qq}^{\mathrm{st}}(\boldsymbol{k}) \end{pmatrix} (2\pi)^2\delta(\boldsymbol{k}_\perp), \tag{61}$$

following the anisotropic approximation (53). Accordingly, eqn (59) and (60) are reduced, respectively, to

$$\Delta\mathcal{C}_{\rho\rho}^{\mathrm{st}}(k_x) = \int \mathrm{d}x \overline{\Delta\mathcal{C}_{\rho\rho}^{\mathrm{st}}}(x) \mathrm{e}^{-ik_x x}, \tag{62}$$

$$\mathcal{C}_{qq}^{\mathrm{st}}(k_x) = \int \mathrm{d}x \overline{\mathcal{C}_{qq}^{\mathrm{st}}}(x) \mathrm{e}^{-ik_x x}, \tag{63}$$

using smeared correlation functions which are integrated over a cross section transverse to the applied electric field:

$$\overline{\Delta\mathcal{C}_{\rho\rho}^{\mathrm{st}}}(x) = \int \mathrm{d}^2\boldsymbol{r}_\perp \Delta\mathcal{C}_{\rho\rho}^{\mathrm{st}}(\boldsymbol{r}), \tag{64}$$

$$\overline{\mathcal{C}_{qq}^{\mathrm{st}}}(x) = \int \mathrm{d}^2\boldsymbol{r}_\perp \mathcal{C}_{qq}^{\mathrm{st}}(\boldsymbol{r}). \tag{65}$$

Correspondingly, the pole eqn (51) and (52) are simplified, respectively, as

$$(k_x^{(1)}\sigma)^2 + (\bar{\kappa}\sigma)^2\omega(k_x^{(1)}) + (pE\sigma)^2 = 0, \tag{66}$$

$$(k_x^{(2)}\sigma)^2 + 0.5(\bar{\kappa}\sigma)^2\omega(k_x^{(2)}) = 0, \tag{67}$$

both of which are different not only from the Debye–Hückel-type equation, $\mathcal{G}_1(\boldsymbol{k}) = 0$, used in equilibrium electrolytes but also from the approximate forms (56) and (57) where $\omega(\boldsymbol{k}) = 1$.

The complex solutions $k_x^{(j)}\sigma$ ($j = 1,2$) to eqn (66) and (67) are related, respectively, to the wavelengths $\mu^{(j)}$ and decaying lengths $\xi_{\mathrm{Decay}}^{(j)}$ of stationary correlation functions at equal times as follows:

$$k_x^{(j)}\sigma = x^{(j)} + iy^{(j)}, \tag{68}$$

$$(x^{(j)}, y^{(j)}) = \left(\frac{2\pi\sigma}{\mu^{(j)}}, \frac{\sigma}{\xi_{\mathrm{Decay}}^{(j)}}\right). \tag{69}$$

Thus, we have clarified that the above expressions (62) and (63) of the anisotropic Fourier transforms satisfy the pole eqn (66) and (67) with eqn (68) and (69). This leads to the averaged correlation functions expressed as

$$\overline{\Delta\mathcal{C}_{\rho\rho}^{\mathrm{st}}}(x) = \sum_{j=1}^{2} A_j \mathrm{e}^{-x/\xi_{\mathrm{Decay}}^{(j)}} \cos\left(\frac{2\pi x}{\mu^{(j)}} + \delta_{\mathrm{a}}^{(j)}\right), \tag{70}$$

$$\overline{\mathcal{C}_{qq}^{\mathrm{st}}}(x) = \sum_{j=1}^{2} B_j \mathrm{e}^{-x/\xi_{\mathrm{Decay}}^{(j)}} \cos\left(\frac{2\pi x}{\mu^{(j)}} + \delta_{\mathrm{b}}^{(j)}\right), \tag{71}$$

where it is noted that both of these density–density and charge–charge correlation functions have the same wavelengths of oscillations in addition to the identical decay lengths, reflecting the above electric-field-induced synchronization.

The introduction of averaged correlation functions given by eqn (64) and (65) enables us to investigate correlations between coarse-grained planes perpendicular to the electric field without consideration of lane formation. In particular, we focus on the pole eqn (66) that predicts an electric-field-induced shift of the Kirkwood crossover from a monotonic decay state to a damped oscillatory state.

More precisely, our focus is on the electric-field-induced Kirkwood crossover between the two regions specified below.

 This journal is © The Royal Society of Chemistry 2022

Open Access Article. Published on 26 May 2022. Downloaded on 7/19/2025 4:45:38 PM.
This article is licensed under a Creative Commons Attribution-NonCommercial 3.0 Unported Licence.

For $\bar{\kappa}\sigma \leq \bar{\kappa}^{(*1)}\sigma$, both solutions to eqn (66) and (67) are purely imaginary: eqn (70) and (71) read

$$\overline{\Delta C_{\rho\rho}^{\mathrm{st}}}(x) = \sum_{j=1}^{2} A_j' \mathrm{e}^{-x/\xi_{\mathrm{Decay}}^{(j)}}, \tag{72}$$

$$\overline{C_{qq}^{\mathrm{st}}}(x) = \sum_{j=1}^{2} B_j' \mathrm{e}^{-x/\xi_{\mathrm{Decay}}^{(j)}}, \tag{73}$$

respectively, where $A_j' = A_j \cos\left(\delta_{\mathrm{a}}^{(j)}\right)$ and $B_j' = B_j \cos\left(\delta_{\mathrm{b}}^{(j)}\right)$. In the range of $\bar{\kappa}\sigma > \bar{\kappa}^{(*1)}\sigma$, on the other hand, the solution to eqn (66) becomes complex while the solution to (67) is purely imaginary: eqn (72) and (73) transform to

$$\begin{aligned}\overline{\Delta C_{\rho\rho}^{\mathrm{st}}}(x) &= A_1 \mathrm{e}^{-x/\xi_{\mathrm{Decay}}^{(1)}} \cos\left(\frac{2\pi x}{\mu^{(1)}} + \delta_{\mathrm{a}}^{(1)}\right) \\ &\quad + A_2' \mathrm{e}^{-x/\xi_{\mathrm{Decay}}^{(2)}},\end{aligned} \tag{74}$$

$$\begin{aligned}\overline{C_{qq}^{\mathrm{st}}}(x) &= B_1 \mathrm{e}^{-x/\xi_{\mathrm{Decay}}^{(1)}} \cos\left(\frac{2\pi x}{\mu^{(1)}} + \delta_{\mathrm{b}}^{(1)}\right) \\ &\quad + B_2' \mathrm{e}^{-x/\xi_{\mathrm{Decay}}^{(2)}},\end{aligned} \tag{75}$$

respectively.

The electric-field-induced Kirkwood crossover is thus represented by the changes of the correlation functions from eqn (72) and (73) to eqn (74) and (75), which occurs at $\bar{\kappa}\sigma = \bar{\kappa}^{(*1)}\sigma$. We further predict the Fisher–Widom crossover[31,36,44] that the density and charge oscillations become obvious in the range of $\bar{\kappa}^{(*1)}\sigma < \bar{\kappa}\sigma < \bar{\kappa}^{(*2)}\sigma$ where the two decay lengths, $\xi_{\mathrm{Decay}}^{(1)}$ and $\xi_{\mathrm{Decay}}^{(2)}$, approach each other; however, it is beyond the scope of this paper to determine the full phase diagram using the steady-state extensions of the Kirkwood and Fisher–Widom crossovers[31] related to eqn (66) and (67).

C. Relationship between *E*-dependent solutions to eqn (66) and the equilibrium decay length

Fig. 2 shows a schematic representation of numerical results presented in Fig. 3 and 8. In Fig. 2, the ratio of $\xi_{\mathrm{Decay}}^{(1)}$ to the smeared Debye–Hückel screening length ξ_{DH} (*i.e.*, $\xi_{\mathrm{Decay}}^{(1)}/\xi_{\mathrm{DH}}$) is shown on a log–log plot as a function of σ/ξ_{DH}.

First, it is seen from Fig. 2 that the equilibrium Kirkwood crossover point[32–36] located at node A shifts gradually along the green arrow with the increase of electric field strength: the dashed green arrow from node A to node B represents the numerical results shown in Fig. 3(b) and 8(b). Incidentally, node B is merely an electric-field-induced Kirkwood crossover point at an arbitrary field strength.

Next, we explain the solid brown curves in Fig. 2 terminated at nodes A and B. These curves represent the $\bar{\kappa}\sigma$-dependencies of $\xi_{\mathrm{Decay}}^{(1)}$ in a uniform state without and with applied electric field, respectively. On the one hand, $\xi_{\mathrm{Decay}}^{(1)}$ at $E = 0$ is identified with ξ_{DH} in the dilute limit of $\bar{\kappa} \sim \bar{n}^{1/2} \to 0$ and decreases more rapidly than ξ_{DH} with increase of $\bar{n}$ in a uniform state prior to the Kirkwood crossover in equilibrium. On the other hand, there are two features as seen from the brown curve under the applied electric field ($E \neq 0$): the dilute limit of $\xi_{\mathrm{Decay}}^{(1)}/\xi_{\mathrm{DH}}$ approaches zero because of the finiteness of the decay length $\xi_{\mathrm{Decay}}^{(1)}$ in the limit of $\xi_{\mathrm{DH}} \to \infty$ as mentioned before, whereas the downward trend of $\xi_{\mathrm{Decay}}^{(1)}/\xi_{\mathrm{DH}}$, similar to the above behavior at $E = 0$, is observed near the electric-field-induced Kirkwood crossover.

Third, let us turn our attention to the dashed blue line in Fig. 2 representing a typical underscreening behavior beyond the Kirkwood line (the vertical blue line through node A) with no electric field applied. The dashed blue line in Fig. 2 depicts the following relation for a decay length ξ_{Decay}:

$$\frac{\xi_{\mathrm{Decay}}}{\xi_{\mathrm{DH}}} \sim \left(\frac{\sigma}{\xi_{\mathrm{DH}}}\right)^{\chi}, \tag{76}$$

$$1 < \chi \leq 2, \tag{77}$$

according to previous simulation and theoretical studies;[20,29–31] the experimental results of $\chi \approx 3$ in RTILs are beyond the scope of this study. It follows from eqn (77) that eqn (76) reads

$$\begin{aligned}&\xi_{\mathrm{Decay}} \sim \bar{n}^{\frac{1-\chi}{2}}, \\ &1 - \chi < 0.\end{aligned} \tag{78}$$

Eqn (78) implies that the decay length ξ_{Decay} of damped oscillations for correlations becomes longer despite increasing $\bar{n}$, which has been referred to as underscreening behavior without an electric field.

Remarkably, the scaling relation given by eqn (76) and (78) applies to the $\bar{\kappa}\sigma$-dependence of $\xi_{\mathrm{Decay}}^{(*1)}/\xi_{\mathrm{DH}}^{(*1)}$ at the Kirkwood crossover; the exponent χ appears close to 1.4 as will be shown in Fig. 3(b).[20,29–31] Reflecting this similarity between the exponents χ of the underscreening behavior and the electric-field-induced shift for $\xi_{\mathrm{Decay}}^{(*1)}$, the dashed blue line in Fig. 2 is drawn as an extension of the green arrow from node A ($E = 0$) to node B ($E \neq 0$).

Last, we focus on the vertical green line through node B in Fig. 2, indicating the condition of the electric-field-induced Kirkwood crossover from a uniform state to a stripe state. In the stripe state, we can observe a damped oscillatory decay of both density–density and charge–charge correlation functions along the direction of applied electric field in the anisotropic approximation (53). It is to be noted here that the stripe state is specified using the averaged correlation functions, $\overline{\Delta C_{\rho\rho}^{\mathrm{st}}}(x)$ and $\overline{C_{qq}^{\mathrm{st}}}(x)$, which by definition smear out density and charge distributions on cross sections perpendicular to the applied electric field (see eqn (64) and (65)).

The emergence of anisotropic density and charge modulations is consistent with the previous results as follows: Theoretically, the SDFT using the Gaussian charge smearing model[35,40] has provided numerical results of two-dimensional correlation functions showing a tendency to form alternating chains of cations and anions along the field direction.[13] Also, according to

Open Access Article. Published on 26 May 2022. Downloaded on 7/19/2025 4:45:38 PM. This article is licensed under a Creative Commons Attribution-NonCommercial 3.0 Unported Licence.

simulation and experimental studies on oppositely charged colloids, the electric-field-driven mixtures have been found to form bands non-parallel to the field direction, other than lanes in the electric field direction, under some conditions on various dynamic phase diagrams of steady states with AC or DC fields applied.[17,18] Our present findings of the emergence of stripe state thus shed light on these anisotropic inhomogeneities as related to crossover phenomena of steady-state correlations.

D. Numerical solutions to eqn (66)

Fig. 3(a) shows the electric-field effects on the Kirkwood crossover in terms of the smeared Debye–Hückel length $\xi_{\mathrm{DH}}^{(*1)}$ and a decay length $\xi_{\mathrm{Decay}}^{(*1)}$ at the Kirkwood crossover. As detailed in Section IV, we have obtained these results using both the Gaussian charge smearing model[35,40] (or the HNC approximation for one-component ionic fluids[42]) and the modified MSA model for the DCF,[43] or its essential function $\omega(\boldsymbol{k})$ given by eqn (12). The former model is depicted by green lines, whereas the latter by red lines. All of the results in Fig. 3(a) exhibit downward trends in accordance with analytical observations made in Section IV.

Furthermore, Fig. 3(a) allows us to make quantitative comparisons between the present two models for the DCF. First, it is confirmed from the values of $\xi_{\mathrm{DH}}^{(*1)}$ at $E = 0$ in Fig. 3(a) that the numerical results correctly reproduce the Kirkwood crossover points previously obtained for the Gaussian charge smearing model[34,35] and the modified MSA model.[29–31,34] Second, Fig. 3(a) shows that the electric-field-induced shifts of $\sigma/\xi_{\mathrm{DH}}^{(*1)}$ are similar to each other. Remembering that $\bar{n}^* = 1/\{8\pi l_{\mathrm{B}}(\xi_{\mathrm{DH}}^{(*1)})^2\}$ by definition (36), it is seen from the variations of $\sigma/\xi_{\mathrm{DH}}^{(*1)}$ in Fig. 3(a) that, irrespective of the models adopted, the crossover densities at $pE\sigma = 3.0$ are evaluated to be less than half of those at $E = 0$. Last, we turn our attention to the relationship between $\xi_{\mathrm{Decay}}^{(*1)}$ and $1/\xi_{\mathrm{DH}}^{(*1)}$ as a function of either $\bar{n}^*$ or E. For a fixed strength of applied electric field, the decay length $\xi_{\mathrm{Decay}}^{(*1)}$ becomes shorter as the ionic solution density $\bar{n}^*$, or $\sigma/\xi_{\mathrm{DH}}^{(*1)}$, becomes larger, which is consistent with the previous results conventionally found for concentrated electrolytes prior to the Kirkwood crossover without an applied electric field.[30–33] The electric-field dependencies, on the other hand, exhibit an opposite relationship between $\xi_{\mathrm{Decay}}^{(*1)}$ and $\xi_{\mathrm{DH}}^{(*1)}$: the downward trends in Fig. 3(a) indicate that both $\xi_{\mathrm{Decay}}^{(*1)}$ and $1/\xi_{\mathrm{DH}}^{(*1)}$ are smaller as E is larger.

Fig. 3(b) demonstrates this opposite tendency using a log–log plot of $\xi_{\mathrm{Decay}}^{(*1)}/\xi_{\mathrm{DH}}^{(*1)}$ *vs.* $\sigma/\xi_{\mathrm{DH}}^{(*1)}$: it is seen from Fig. 3(b) that

$$\frac{\xi_{\mathrm{Decay}}^{(*1)}}{\xi_{\mathrm{DH}}^{(*1)}} \sim \left(\frac{\sigma}{\xi_{\mathrm{DH}}^{(*1)}}\right)^{\chi} \tag{79}$$

for an exponent χ larger than unity. The dotted line is a guide to the eye, indicating that χ is close to 1.4 and is consistent with the relation $1 < \chi \leq 1.5$ previously obtained from simulation results on underscreening behaviors in RTILs beyond the Kirkwood line with no electric field applied.[20,29–31]

E. The 2D inverse Fourier transforms for assessing the anisotropic approximation (53)

The last subsection of Section III presents the results of the 2D inverse Fourier transforms using heat maps, which would help us not only to understand the above analytical results concretely but also to assess the anisotropic approximation (53). We perform the 2D inverse Fourier transform of $\Delta\mathcal{C}_{\rho\rho}^{\mathrm{st}}(k_x, k_y)$ by setting $k_z = 0$ similar to the expressions (61), (62) and (64):

$$\Delta\mathcal{C}_{\rho\rho}^{\mathrm{st}}(k_x, k_y) = \iint \mathrm{d}x\mathrm{d}y\overline{\Delta\mathcal{C}_{\rho\rho}^{\mathrm{st}}}(x, y)\mathrm{e}^{-ik_x x - ik_y y}, \tag{80}$$

$$\overline{\Delta\mathcal{C}_{\rho\rho}^{\mathrm{st}}}(x, y) \equiv \int \mathrm{d}z\Delta\mathcal{C}_{\rho\rho}^{\mathrm{st}}(\boldsymbol{r}). \tag{81}$$

In other words, the inverse Fourier transform provides the mean correlation function $\overline{\Delta\mathcal{C}_{\rho\rho}^{\mathrm{st}}}(x, y)$ as follows:

$$\overline{\Delta\mathcal{C}_{\rho\rho}^{\mathrm{st}}}(x, y) = \frac{1}{(2\pi)^2}\iint \mathrm{d}k_x\mathrm{d}k_y\Delta\mathcal{C}_{\rho\rho}^{\mathrm{st}}(k_x, k_y)\mathrm{e}^{ik_x x + ik_y y}. \tag{82}$$

The 2D results of the mean correlation function $\overline{\Delta\mathcal{C}_{\rho\rho}^{\mathrm{st}}}(x, y)$ can reflect the 3D behaviors of density–density correlations when the translational symmetry of $\Delta\mathcal{C}_{\rho\rho}^{\mathrm{st}}(\boldsymbol{r})$ is preserved with respect to the z-direction and the correlation functions on the xy cross-sections are indistinguishable at two different z values.

The setup in Fig. 1 is a plausible example to satisfy such translational symmetry. The upper figure of Fig. 1 indicates that the plate-plate distance is sufficiently smaller than the size in the z-direction, and yet we suppose that the finite-size effects are negligible because the plate-plate distance is much larger than the sphere diameter as mentioned in Section IIA. Such a system could serve as a platform for investigating the 2D inverse Fourier transforms of the 3D primitive model.

We also compare the 1D results of the mean correlation functions, $\overline{\Delta\mathcal{C}_{\rho\rho}^{\mathrm{st}}}(x, y_0)$ at a fixed y-coordinate value of y_0 and $\overline{\Delta\mathcal{C}_{\rho\rho}^{\mathrm{st}}}(x)$ defined by eqn (64), which are related respectively to the 2D mean correlation function $\overline{\Delta\mathcal{C}_{\rho\rho}^{\mathrm{st}}}(x, y)$ defined by eqn (81) as follows:

$$\overline{\Delta\mathcal{C}_{\rho\rho}^{\mathrm{st}}}(x, y_0) = \int \mathrm{d}y\overline{\Delta\mathcal{C}_{\rho\rho}^{\mathrm{st}}}(x, y)\delta(y - y_0), \tag{83}$$

$$\overline{\Delta\mathcal{C}_{\rho\rho}^{\mathrm{st}}}(x) = \int \mathrm{d}y\overline{\Delta\mathcal{C}_{\rho\rho}^{\mathrm{st}}}(x, y), \tag{84}$$

revealing that $\overline{\Delta\mathcal{C}_{\rho\rho}^{\mathrm{st}}}(x = 0, y_0) < \overline{\Delta\mathcal{C}_{\rho\rho}^{\mathrm{st}}}(x = 0)$ because of $\overline{\mathcal{C}_{\rho\rho}^{\mathrm{st}}}(x = 0) = \overline{\Delta\mathcal{C}_{\rho\rho}^{\mathrm{st}}}(x = 0, y_0)\int \mathrm{d}y\overline{\Delta\mathcal{C}_{\rho\rho}^{\mathrm{st}}}(x = 0, y)$ (see Fig. 5 for confirmation).

Below we provide results of the inverse Fourier transforms in Fig. 4–6, demonstrating real-space behaviors of the density–density correlation function in a high-density region such that $\bar{\kappa}\sigma$ exceeds the Fisher–Widom-like crossover[31,36,44] as well as the Kirkwood crossover:[32–36] $\bar{\kappa}\sigma > \bar{\kappa}^{(*2)}\sigma$ $(> \bar{\kappa}^{(*1)}\sigma)$ is

 This journal is © The Royal Society of Chemistry 2022

Open Access Article. Published on 26 May 2022. Downloaded on 7/19/2025 4:45:38 PM.
This article is licensed under a Creative Commons Attribution-NonCommercial 3.0 Unported Licence.

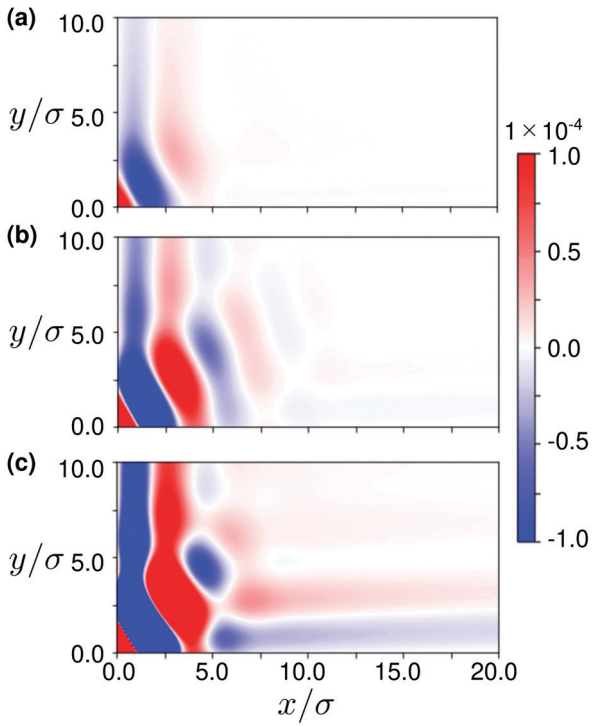

Fig. 4 Comparison between the 2D results of $\overline{\Delta\mathcal{C}^{\mathrm{st}}_{\rho\rho}}(x,y)$ for different conditions on ionic condition and electric field strength. The color bar on the right hand side, which is common to the three heat maps, represents the value of $\overline{\Delta\mathcal{C}^{\mathrm{st}}_{\rho\rho}}(x,y)$ at a location (x/σ, y/σ) measured in units of sphere diameter σ. While the difference between Fig. 4(a) and (b) is ionic concentration, or $\bar{\kappa}\sigma$, at an identical electrical field, an electric field effect is seen from comparing Fig. 4(b) and (c) at a same ionic concentration: (a) ($\bar{\kappa}\sigma$, $pE\sigma$) = (2.2,0.5); (b) ($\bar{\kappa}\sigma$, $pE\sigma$) = (2.6,0.5); (c) ($\bar{\kappa}\sigma$, $pE\sigma$) = (2.6,1.5).

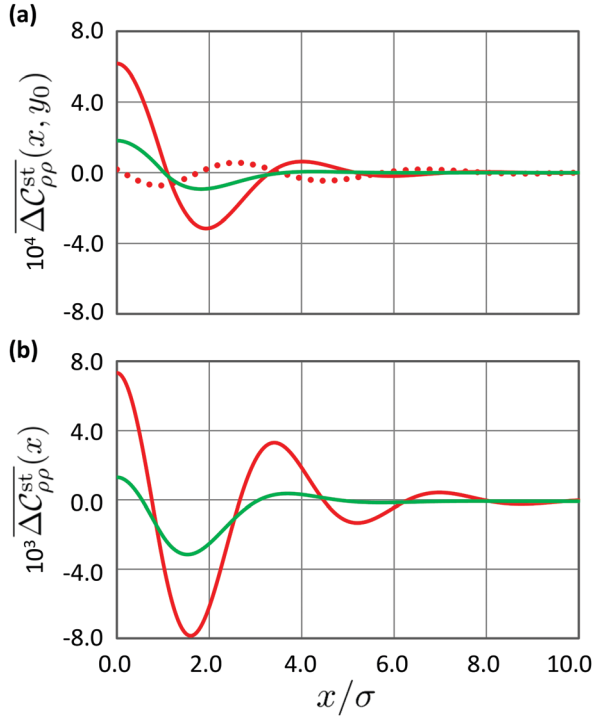

Fig. 5 Comparison between the 1D results of $\overline{\Delta\mathcal{C}^{\mathrm{st}}_{\rho\rho}}(x,y_0)$ at a fixed y-coordinate value of y_0 and $\overline{\Delta\mathcal{C}^{\mathrm{st}}_{\rho\rho}}(x)$ defined by eqn (64). The density–density correlation functions are plotted as functions of x/σ, the separation distance in the applied field direction measured in units of sphere diameter σ. At an identical electric field strength $pE\sigma$ = 0.5, two ionic concentrations, $\bar{\kappa}\sigma$ = 2.2 and 2.6, are considered in both figures: (a) the green and red solid lines depict the behaviors of $\overline{\Delta\mathcal{C}^{\mathrm{st}}_{\rho\rho}}(x,y_0=0)$ at $\bar{\kappa}\sigma$ = 2.2 (green) and 2.6 (red), respectively, whereas the red dotted line represents $\overline{\Delta\mathcal{C}^{\mathrm{st}}_{\rho\rho}}(x,y_0=5\sigma)$ at $\bar{\kappa}\sigma$ = 2.6; (b) the green and red solid lines depict the behaviors of $\overline{\Delta\mathcal{C}^{\mathrm{st}}_{\rho\rho}}(x)$ at $\bar{\kappa}\sigma$ = 2.2 and 2.6, respectively.

investigated (remember the discussion at the end of Section IIB). We see from Fig. 4 that stripe states illustrated in Fig. 2 are observed more clearly as $\bar{\kappa}\sigma$ is larger at a fixed strength of electric field. In Fig. 5 and 6, we validate the anisotropic approximation (53) from comparing $\overline{\Delta\mathcal{C}^{\mathrm{st}}_{\rho\rho}}(x,y_0)$ and $\overline{\Delta\mathcal{C}^{\mathrm{st}}_{\rho\rho}}(x)$ (see also eqn (83) and (84)). Furthermore, Fig. 7 shows the emergence of a lane structure with the increase of electric field strength from $pE\sigma$ = 0.1 to 1.0 at a high value of $\bar{\kappa}\sigma$ = 2.78.

Fig. 4 shows how the density–density correlation behaviors vary depending on the ionic concentration and electric field strength. The difference between Fig. 4(a) and (b) is the ionic concentration at the same electric field of $pE\sigma$ = 0.5. Meanwhile, the difference between Fig. 4(b) and (c) is the strength of electric field at the same ionic condition of $\bar{\kappa}\sigma$ = 2.6. Fig. 4(b) can be a reference result for investigating the effects of ionic concentration and electric field strength. Fig. 4(b) exhibits the oscillatory decay behaviors in the external field direction on an xy plane, which is typical of density–density correlations in the stripe state.

When $\bar{\kappa}\sigma$ is reduced from 2.6 to 2.2 without changing the electric field strength, we obtain the result of Fig. 4(a). Comparison between Fig. 4(a) and (b) indicates the following. First, we can observe the oscillatory decays in the external field direction for both values of $\bar{\kappa}\sigma$ when setting the electric field

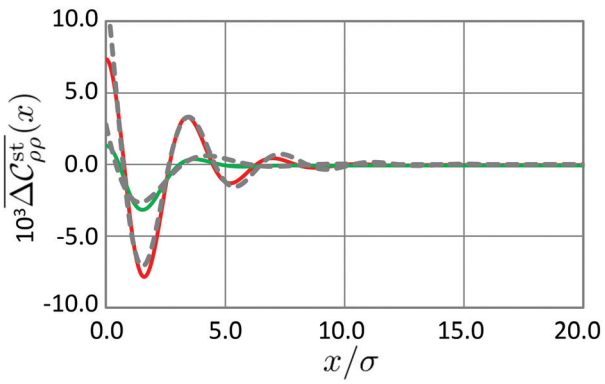

Fig. 6 The green and red lines are the same results as those in Fig. 5(b): we show $\overline{\Delta\mathcal{C}^{\mathrm{st}}_{\rho\rho}}(x)$ over the range, $0 \le x/\sigma \le 20$, at $\bar{\kappa}\sigma$ = 2.2 (green) and 2.6 (red) in the presence of applied electric field ($pE\sigma$ = 0.5). The dashed lines correspond to the best fit of eqn (85).

strength to be $pE\sigma$ = 0.5. Furthermore, Fig. 4(a) shows that the correlation function becomes almost zero for $x \ge 5\sigma$: The density–density correlation function becomes equal to $2\bar{n}\delta(\boldsymbol{r})$

Open Access Article. Published on 26 May 2022. Downloaded on 7/19/2025 4:45:38 PM.
This article is licensed under a Creative Commons Attribution-NonCommercial 3.0 Unported Licence.

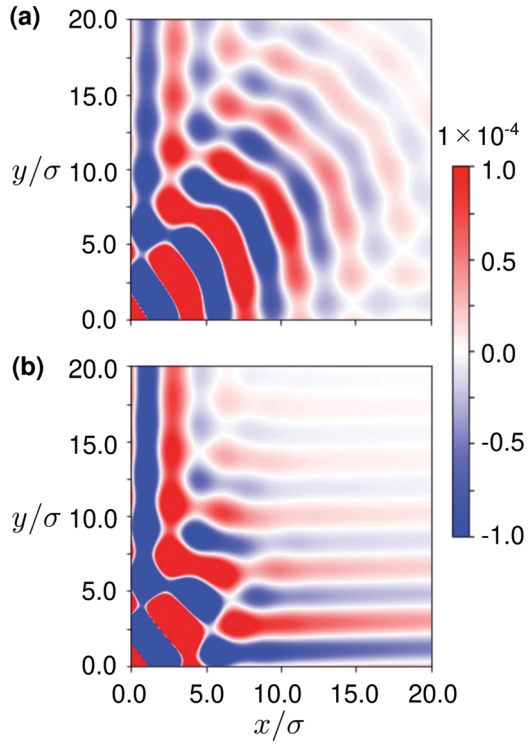

Fig. 7 Comparison between the 2D results of $\overline{\Delta C^{st}_{\rho\rho}}(x,y)$ at different electric field strengths: (a) $pE\sigma$ = 0.1 and (b) $pE\sigma$ = 1.0. The same ionic condition $\bar{\kappa}\sigma$ = 2.78 is adopted in both results.

for $x \geq 5\sigma$ in contrast to the long-range correlations seen in Fig. 4(b). The different behaviors of density–density correlations suggest that the smaller $\bar{\kappa}\sigma$ is, the shorter the decay length becomes. In other words, comparison between Fig. 4(a) and (b) reveals an underscreening behavior[19,20,29–31] beyond the Kirkwood condition as depicted in the schematic of Fig. 2. Fig. 4(c) further demonstrates that alignment of segregation band to the external field direction becomes clear by increasing the electric field strength to $pE\sigma$ = 1.5 at $\bar{\kappa}\sigma$ = 2.6.

Fig. 4 has found an external field condition ($pE\sigma$ = 0.5) that creates an anisotropic density modulation reflecting the stripe state as depicted in Fig. 2. This finding has justified the anisotropic approximation (53) from a qualitative point of view. We make below a quantitative assessment of the anisotropic approximation (53). To this end, we further investigate the extent to which the one-variable correlation function represents the results of Fig. 4 using Fig. 5 and 6.

Fig. 5 compares the x-dependencies of the 2D correlation function $\overline{\Delta C^{st}_{\rho\rho}}(x,y_0)$ at y_0, a fixed y-coordinate value, with the behaviors of the one-variable correlation function $\overline{\Delta C^{st}_{\rho\rho}}(x)$ defined by eqn (64). Both solid lines in Fig. 5(a) show the x-dependencies at y_0 = 0. The same external field condition $pE\sigma$ = 0.5 is used in both results of Fig. 5(a) and (b), and the ionic conditions for the green and red lines are identical in Fig. 5(a) and (b): the green and red lines represent the results at $\bar{\kappa}\sigma$ = 2.2 and 2.6, respectively.

It is noted that the value of the vertical axis in Fig. 5(a) is one-tenth of that in Fig. 5(b) due to the different definitions of the two correlation functions as clarified by eqn (83) and (84). Nevertheless, the behaviors bear resemblances. First, these two functions, $\overline{\Delta C^{st}_{\rho\rho}}(x,y_0)$ and $\overline{\Delta C^{st}_{\rho\rho}}(x)$, exhibit oscillatory decay behaviors, and we will make a quantitative comparison using Fig. 6. They also share the feature of correlation value that becomes smaller with the decrease of ionic concentration from $\bar{\kappa}\sigma$ = 2.6 to 2.2. Furthermore, we observe that the oscillations disappear faster for the green line than for the red line in both Fig. 5(a) and (b), which corresponds to the underscreening behavior suggested by Fig. 4.

The solid lines in Fig. 5(a) are the results at a fixed y-coordinate: y_0 = 0. The specific value of y_0 raises the question as to whether or not the above similarity of solid lines in Fig. 5(a) and (b) is a coincidence. To address this question, the red dashed line shows the x-dependency of the two-variable function at y_0/σ = 5 when $pE\sigma$ = 0.5 and $\bar{\kappa}\sigma$ = 2.2. We can see that the period of the dashed red line is close to that of the solid red line. However, the initial phase is different from that at y_0/σ = 0, and the correlation value is reduced considerably even at x/σ = 0 as y_0/σ varies from 0 to 5. The latter difference implies that the x-dependency of $\overline{\Delta C^{st}_{\rho\rho}}(x,y_0)$ near y_0/σ = 0 greatly contributes to the one-variable correlation function $\overline{\Delta C^{st}_{\rho\rho}}(x)$ defined by eqn (64), which is why the two solid lines in Fig. 5(a) reproduce the one-variable function behaviors in Fig. 5(b).

Let us consider a simple asymptotic form determined by a single decay length ξ_{Decay} and oscillation period μ:

$$\overline{\Delta C^{st}_{\rho\rho}}(x) = A e^{-x/\xi_{Decay}} \cos\left(\frac{2\pi x}{\mu} + \delta_a\right), \qquad (85)$$

which is fitted to the results of Fig. 5(b) instead of eqn (70). While the solid lines in Fig. 6, which are the same as those of Fig. 5(b), are shown over the range $0 \leq x/\sigma \leq 20$, the dashed lines in Fig. 6 correspond to the best fit of eqn (85). The best-fit parameter sets are as follows:(A, ξ_{Decay},μ, δ_a) = (0.6×10^{-2}, 2.0, 5.6, 1.1) at $\bar{\kappa}\sigma$ = 2.2, whereas (A, ξ_{Decay},μ, δ_a) = (1.3×10^{-2}, 2.5, 3.8, 0.4) at $\bar{\kappa}\sigma$ = 2.6. The best-fit periods, μ = 5.6 and 3.8, reflect the oscillatory behaviors seen from Fig. 6. Meanwhile, the best-fit decay length ξ_{Decay} extends from 2σ to 2.5σ with the increase of $\bar{\kappa}\sigma$ from 2.2 to 2.6, which is a quantitative result of underscreening behavior. Evaluating the exponent χ defined by eqn (79) from this increase in ξ_{Decay}, we have $2 < \chi < 3$; it is interesting to note that the present exponent is larger than the equilibrium exponent ($1 < \chi \leq 1.5$) previously obtained from the MSA of the 3D primitive model but is close to the exponent experimentally obtained.[19]

Last, we consider the 2D inverse Fourier transforms of $\overline{\Delta C^{st}_{\rho\rho}}(x,y)$ when increasing $\bar{\kappa}\sigma$ to 2.78. The strengths of the applied electric field are $pE\sigma$ = 0.1 (Fig. 7(a)) and $pE\sigma$ = 1.0 (Fig. 7(b)). The heat maps in Fig. 7 reveal the oscillatory 2D patterns due to the suppression of decaying behaviors. On the one hand, even at the weak electric field strength of $pE\sigma$ = 0.1, Fig. 7(a) shows that segregation bands of ions with the same sign are deformed along the x-axis, the external field direction, though the stripe state remains a good approximation in the

 This journal is © The Royal Society of Chemistry 2022

Open Access Article. Published on 26 May 2022. Downloaded on 7/19/2025 4:45:38 PM.
This article is licensed under a Creative Commons Attribution-NonCommercial 3.0 Unported Licence.

region of $y/\sigma \leq 5$. On the other hand, at $pE\sigma = 1.0$, Fig. 7(b) demonstrates the emergence of lane structure formed by aligned bands, revealing that the anisotropic approximation (53) becomes invalid far beyond the electric-field-induced Kirkwood crossovers.

IV. Details on the determination of the electric-field-induced Kirkwood crossovers in the anisotropic approximation

We perform the correlation function analysis, especially focusing on the pole eqn (66). In Section IVA, we see that discriminant analysis of a quadratic equation becomes available to investigate the solution to eqn (66), irrespective of the function forms of $\omega(\boldsymbol{k})$, as a result of the small $k_x\sigma$-expansion of the key function $\omega(\boldsymbol{k})$. Section IVB provides concrete results of both the Gaussian charge smearing model and the modified MSA model for clarifying how the results in Fig. 3 are obtained.

A. A general approximation of eqn (66) for evaluating the Kirkwood crossover point

Expanding $\omega(\boldsymbol{k})$ with respect to $k_x^{(1)}\sigma$, we have a general form,

$$\omega(k_x^{(1)}) \approx 1 - \alpha_1(k_x^{(1)}\sigma)^2 + \alpha_2(k_x^{(1)}\sigma)^4, \tag{86}$$

as seen from eqn (12); for instance, $\alpha_1 = 1/2$ and $\alpha_2 = 1/8$ for the Gaussian charge smearing model,[35,40] and $\alpha_1 = 1/2$ and $\alpha_2 = 1/24$ for the modified MSA model.[43] Eqn (66) then reduces to the quadratic equation for $\mathcal{S} \equiv (k_x^{(1)}\sigma)^2$:

$$\alpha_2\overline{\kappa}^2\sigma^2\mathcal{S}^2 + (1 - \alpha_1\overline{\kappa}^2\sigma^2)\mathcal{S} + \overline{\kappa}^2\sigma^2 + (pE)^2\sigma^2 = 0. \tag{87}$$

It follows from eqn (68) that

$$(k_x^{(1)}\sigma)^2 = x^2 - y^2 + 2ixy \tag{88}$$

where x and y are related to the decay length $\xi_{\mathrm{Decay}}^{(1)}$ and wavelength $\mu^{(1)}$ as defined in eqn (69). Eqn (69) and (88) imply that discriminant analysis of eqn (87) is found useful to determine the Kirkwood crossover point where the correlation functions change from monotonic ($\mu^{(1)} = 0$) to oscillatory ($\mu^{(1)} \neq 0$) decay. As mentioned in eqn (54), the imaginary solution $2ixy$ disappears at $\overline{\kappa}^{(*1)}\sigma$ because of $x = 0$, or $\mu^{(1)} \to \infty$: the Kirkwood crossover occurs when exceeding $\overline{\kappa}^{(*1)}\sigma$.

We find approximate forms of the solution to the discriminant equation of eqn (87) as follows:

$$\left(\overline{\kappa}^{(*1)}\sigma\right)^2 = \frac{1 - \sqrt{\alpha_2}(pE)^2\sigma^2}{\alpha_1 + 2\sqrt{\alpha_2}} \quad (pE\sigma \ll 1) \tag{89}$$

$$\to 0 \quad (pE\sigma \gg 1); \tag{90}$$

see Appendix E for these derivations. Plugging the modified MSA coefficients, $\alpha_1 = 1/2$ and $\alpha_2 = 1/24$, into the relation (89) for $E = 0$, we have

$$\overline{\kappa}^{(*1)}\sigma = \left(\frac{1}{\alpha_1 + 2\sqrt{\alpha_2}}\right)^{1/2} \approx 1.05, \tag{91}$$

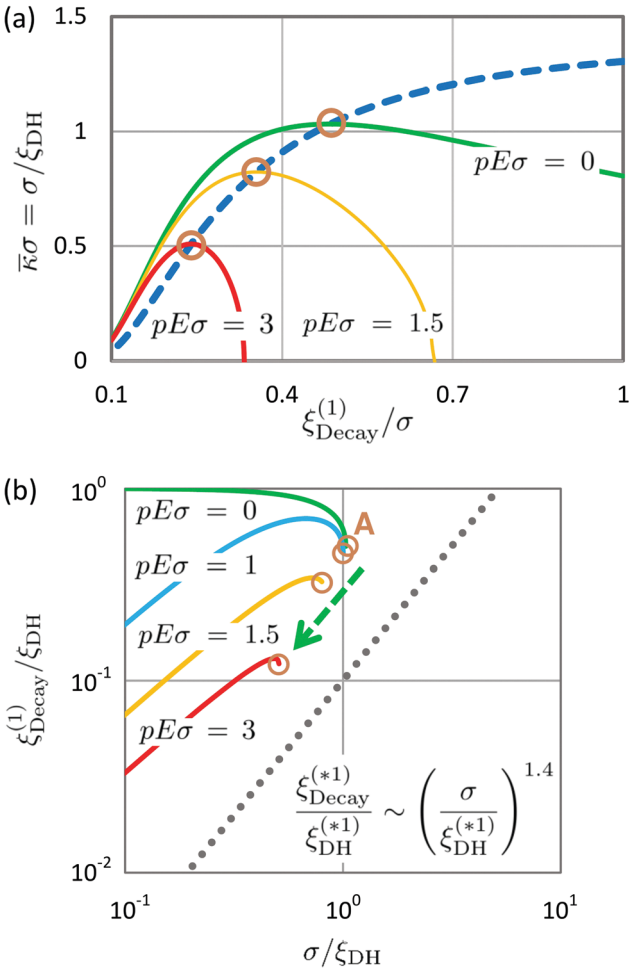

Fig. 8 Comparison between Fig. 2 (a schematic summary) and numerical results of the modified MSA model. (a) The graphical representation of the solution to $u(y^*) = v(y^*)$ given by eqn (105) and (106), respectively. Eqn (105) provides $\overline{\kappa}\sigma = \sqrt{u(y = \sigma/\xi_{\mathrm{Decay}}^{(1)})}$, the $\xi_{\mathrm{Decay}}^{(1)}$-dependence of $\overline{\kappa}\sigma$, which varies depending on the electric field strength measured by $pE\sigma$. The colored solid lines represent these dependencies for $pE\sigma = 0$ (green), $pE\sigma = 1.5$ (orange), and $pE\sigma = 3$ (red). Meanwhile, the blue dashed line shows another dependence of $\overline{\kappa}\sigma$ on $\xi_{\mathrm{Decay}}^{(1)}/\sigma$ which is given by $\overline{\kappa}\sigma = \sqrt{v(y)}$ (see eqn (106)). The three intersection points are indicated by brown circles, giving both the Debye–Hückel lengths $\xi_{\mathrm{DH}}^{(*1)}$ at the electric-field-induced crossovers and the Kirkwood decay lengths $\xi_{\mathrm{Decay}}^{(*1)}$ at different field strengths. (b) Numerical results summarized in Fig. 2. In this figure, the $\overline{\kappa}\sigma$-dependencies of $\xi_{\mathrm{Decay}}^{(1)}$ are depicted by the solid lines colored green ($pE\sigma = 0$), blue ($pE\sigma = 1$), orange ($pE\sigma = 1.5$), and red ($pE\sigma = 3$), from top to bottom, on a log–log plot of $\xi_{\mathrm{Decay}}^{(1)}/\xi_{\mathrm{DH}} = \overline{\kappa}\xi_{\mathrm{Decay}}^{(1)}$ *vs.* $\sigma/\xi_{\mathrm{DH}} = \overline{\kappa}\sigma$. The brown circles mark the termination points of these lines representing the Kirkwood crossover points at each electric-field strength, and the rightmost circle A corresponds to node A in Fig. 2, the Kirkwood crossover point at $E = 0$. The location shift of brown circles with the increase of E is indicated by the dashed green arrow, showing an electric-field-induced shift of the Kirkwood crossover. For comparison, the dotted line delineates the scaling relation, $\xi_{\mathrm{Decay}}^{(*1)}/\xi_{\mathrm{DH}}^{(*1)} \sim (\sigma/\xi_{\mathrm{DH}}^{(*1)})^{1.4}$, as well as that in Fig. 3(b).

which is in good agreement with the Kirkwood crossover values previously obtained for the primitive model in the absence of applied electric field.[29–33]

Eqn (89) and (90) imply that the Debye–Hückel length $\xi_{\mathrm{DH}}^{(*1)} = 1/\overline{\kappa}^{(*1)}$ at the Kirkwood crossover becomes longer as E is larger.

Open Access Article. Published on 26 May 2022. Downloaded on 7/19/2025 4:45:38 PM.
This article is licensed under a Creative Commons Attribution-NonCommercial 3.0 Unported Licence.

Namely, the crossover density $\bar{n}^* = 1/\{8\pi l_B(\xi_{DH}^{(*1)})^2\}$ becomes lower with the increase of E; eqn (90) predicts that both charge–charge and density–density oscillations are observed even in a dilute electrolyte upon applying a high electric field.

B. Analytical and numerical results

Gaussian charge smearing model.[35,40] First, we consider the Gaussian charge smearing model. This model is represented by $\omega(k_x^{(1)}\sigma) = e^{-(k_x^{(1)}\sigma)^2/2}$ in eqn (12). Then, eqn (66) is rewritten as

$$2\tau e^{\frac{\left(k_x^{(1)}\sigma\right)^2}{2}} + \bar{\kappa}^2\sigma^2 = 0, \tag{92}$$

$$2\tau = (k_x^{(1)}\sigma)^2 + (pE)^2\sigma^2. \tag{93}$$

It is convenient to transform eqn (92) and (93) to

$$e^{\tau}\tau = -\frac{\bar{\kappa}^2\sigma^2}{2}e^{\frac{(pE)^2\sigma^2}{2}}, \tag{94}$$

$$2\tau = x^2 - y^2 + (pE)^2\sigma^2 + 2ixy, \tag{95}$$

which can be rewritten as

$$\tau = \mathcal{W}\left(-\frac{\bar{\kappa}^2\sigma^2}{2}e^{\frac{(pE)^2\sigma^2}{2}}\right), \tag{96}$$

using the Lambert function $\mathcal{W}$[35] defined by $\tau = \mathcal{W}(\tau e^{\tau})$.

Focusing on the principal branch of the Lambert function,[35] it is found that the Kirkwood crossover point satisfies the relations,

$$\frac{(\bar{\kappa}^{(*1)}\sigma)^2}{2}e^{\frac{(pE)^2\sigma^2}{2}} = 1/e, \tag{97}$$

$$\tau^* = -1, \tag{98}$$

similar to those at $E = 0$. Eqn (97) transforms to

$$\bar{\kappa}^{(*1)}\sigma = e^{-\frac{(pE)^2\sigma^2}{4}}\sqrt{\frac{2}{e}} \tag{99}$$

or

$$\bar{n}^* = \left(\frac{1}{4\pi p^2 l_B\sigma^2}\right)e^{-\frac{(pE)^2\sigma^2}{2}-1} \tag{100}$$

for the crossover density $\bar{n}^*$. Eqn (99) verifies the above approximate result (90), whereas eqn (100) enables us to make an analytical prediction that the increase of E results in the decrease of $\bar{n}^*$. Inserting eqn (98) into eqn (95), we have

$$-2 = -\left(\frac{\sigma}{\xi_{Decay}^{(*1)}}\right)^2 + (pE)^2\sigma^2, \tag{101}$$

or

$$\frac{\xi_{Decay}^{(*1)}}{\sigma} = \frac{1}{\sqrt{2 + (pE)^2\sigma^2}}, \tag{102}$$

because of $x = 0$ at the Kirkwood crossover. Eqn (100) and (102) state that, as E is larger, Coulomb interactions are more short-ranged despite the decrease in the Kirkwood crossover density $\bar{n}^*$ given by eqn (100). In other words, our target mode $k_x^{(*1)}$ describes an aspect of electric-field-induced screening which is enhanced by the applied electric field (see also the last paragraph of Section IIIA for the underlying physics).

The modified MSA model.[43] Next, we adopt $\omega(\boldsymbol{k}) = \cos(k_x^{(1)}\sigma)$ and the strong-coupling approximation of the modified MSA model (see Section IVB). Bearing in mind that $\cos(k_x^{(1)}\sigma) = \cos x\cosh y - i\sin x\sinh y$, eqn (66) reads

$$\bar{\kappa}^2\sigma^2\cos x\cosh y = y^2 - (pE)^2\sigma^2 - x^2, \tag{103}$$

$$\bar{\kappa}^2\sigma^2\sin x\sinh y = 2xy, \tag{104}$$

for the real and imaginary parts, respectively. The Kirkwood crossover occurs in the limit of $x \to 0$ (or $\mu^{(1)} \to \infty$). In this limit, eqn (103) and (104) reduce to

$$(\bar{\kappa}^{(*1)}\sigma)^2 = u(y^*) = \frac{(y^*)^2 - (pE)^2\sigma^2}{\cosh y^*}, \tag{105}$$

$$= v(y^*) = \frac{2y^*}{\sinh y^*}, \tag{106}$$

for $y^* = \sigma/\xi_{Decay}^{(*1)}$.

Fig. 8(a) shows the curves of $\bar{\kappa}\sigma = \sqrt{u(y)}$ and $\bar{\kappa}\sigma = \sqrt{v(y)}$ as a function of $y = \sigma/\xi_{Decay}^{(1)}$ including the Kirkwood crossover value y^*. While there is a single line of $\bar{\kappa}\sigma = \sqrt{v(y)}$ in Fig. 8(a), the curves of $\bar{\kappa}\sigma = \sqrt{u(y)}$ are depicted using different values of $pE\sigma$ = 0, 1.5 and 3. We can see from Fig. 8(a) that the intersection points of these curves (three brown circles located at the intersections in Fig. 8(a)) is determined by $u(y^*) = v(y^*)$ and is located at the maximum of $\bar{\kappa}\sigma = \sqrt{u(y)}$ as a function of y; actually, it is easily confirmed that $u(y^*) = v(y^*)$ is nothing but the maximum condition for $\bar{\kappa}\sigma = \sqrt{u(y)}$. We find from a series of intersection points $(y^*, \sqrt{u(y^*)})$ for different field strengths in Fig. 8(a) that the modified MSA model[43] exhibits a similar trend observed in the above Gaussian charge smearing model:[35] the maxima of $\bar{\kappa}\sigma = \sqrt{u(y)}$ decrease with increase of E. That is, the Debye–Hückel length $\xi_{DH}^{(*1)}$ at the electric-field-induced crossover is larger as the decay length $\xi_{Decay}^{(*1)}$ at the Kirkwood crossover is smaller due to the increase of E. These dependencies are in qualitative agreement with eqn (99) and (102) of the Gaussian charge smearing model.

Relationship between the results in Fig. 8 and the present results given by eqn (99), (102), (105) and (106). Thus, we have obtained the formulation to find the results in Fig. 8(a). On the one hand, eqn (99) and (102) yield $\sigma/\xi_{DH}^{(*1)}$ (or $\bar{\kappa}^{(*1)}\sigma$) and $\xi_{Decay}^{(*1)}/\sigma$ of the Gaussian charge smearing model, respectively. On the other hand, eqn (105) and (106) are solved numerically to find $k_x^{(*1)}\sigma$, or the inverse of $\xi_{Decay}^{(*1)}/\sigma$ in the modified MSA,[43] and we can easily calculate $\bar{\kappa}^{(*1)}\sigma$ from $\xi_{Decay}^{(*1)}/\sigma$ using eqn (105). The same results as those of Fig. 8(a) are presented on a log–log

 This journal is © The Royal Society of Chemistry 2022

Open Access Article. Published on 26 May 2022. Downloaded on 7/19/2025 4:45:38 PM. This article is licensed under a Creative Commons Attribution-NonCommercial 3.0 Unported Licence.

plot in Fig. 8(b), further indicating that, in the range of $10^{-1} < \sigma/\xi_{DH}^{(*1)} < 10^{0}$, the $\sigma/\xi_{DH}^{(*1)}$-dependencies of $\xi_{Decay}^{(*1)}/\xi_{DH}^{(*1)}$ exhibit a scaling relation $\xi_{Decay}^{(*1)}/\xi_{DH}^{(*1)} \sim (\sigma/\xi_{DH}^{(*1)})^{\chi}$ with χ being close to 1.4, which is similar to eqn (76) previously found for concentrated electrolytes.[20,29–31]

V Discussion and conclusions

This paper has demonstrated the usefulness of the SDFT[13–15] on concentrated electrolytes under steady electric fields, which is summarized in Table 1 and Fig. 2. While Table 1 has provided a detailed summary of our stochastic mPNP model in comparison with previous mPNP models,[5–15] we would like to make additional three remarks related to the schematic summary of Fig. 2.

(i) The weight function $\omega(k)$ in terms of the Kirkwood crossover

It has been proved that we can extend the mPNP models to consider the stochastic process, thereby allowing us to obtain stationary equal-time correlation functions which include the key function $\omega(\boldsymbol{k})$ as seen from eqn (43)–(48). To be noted, the Kirkwood crossover does not occur without $\omega(\boldsymbol{k})$ given by eqn (12); therefore, it is indispensable to incorporate either the finite-spread Poisson eqn (14) or the generalized Debye–Hückel eqn (17) into the stochastic mPNP models for predicting the onset of oscillatory decay of correlations.

(ii) Stripe states

An oscillatory state along the field direction (a stripe state) as given in Fig. 2 is stationary as long as lane formation is not favored. The stripe state is consistent with some previous findings of inhomogeneous steady states such as alternating chains of cations and anions along the applied field direction in electrolytes[13] and non-parallels bands in oppositely charged colloidal mixtures[17,18] (see the last paragraph of Section IIIC). Incidentally, it has been found that the lane structure[17] clearly appears in concentrated electrolytes at a moderate condition such that $\bar{\kappa}\sigma \approx 1.6$ and $p^2 l_B/\sigma = 1$ by adding to the mPNP equations a fluctuating advection term due to interparticle interactions.[45]

(iii) Fisher–Widom crossover between two Kirkwood crossovers

Above the Kirkwood crossover condition of $\bar{\kappa}\sigma > \bar{\kappa}^{(*1)}\sigma$, we have smeared correlation functions, $\overline{\Delta C_{\rho\rho}^{st}}(x)$ and $\overline{C_{qq}^{st}}(x)$, which are given by the sum of oscillatory and monotonic decay functions (*i.e.*, eqn (74) and (75)). Furthermore, the monotonic decay parts of correlation functions subsequently become oscillatory when $\bar{\kappa}\sigma$ goes beyond $\bar{\kappa}^{(*2)}\sigma$ which is related to the equilibrium Kirkwood crossover value $\bar{\kappa}^{*}\sigma$ as eqn (55). This crossover phenomenon suggests the possibility of simultaneous occurrence of the Fisher–Widom crossover[31,36,44] for density–density and charge–charge correlations in the range of $\bar{\kappa}^{(*1)}\sigma \le \bar{\kappa}\sigma \le \bar{\kappa}^{(*2)}\sigma$ though the full phase diagram of steady states for electric-field-driven electrolytes remains to be determined. For the concrete understanding of anisotropic density modulations in stripe states, Section IIIE presents various results on the 2D density–density correlations beyond the Fisher–Widom crossover. As confirmed from Fig. 4 and 7, there are some electric field conditions that create stripe states formed by segregation bands transverse to the external field direction.

It is still necessary to investigate whether experimental and simulation studies can find an electric-field-induced shift of the Kirkwood crossover from monotonic to oscillatory decay of density–density and charge–charge correlations in the applied electric field direction. Therefore, let us make three comparisons in terms of realizability.

Although the primitive model has been used for investigating concentrated electrolytes, we would like to see the interaction parameters of RTILs and colloidal nano-particle dispersions as well as concentrated electrolytes. For instance, let us consider $(p, \sigma, \varepsilon, l_B) = (1, 0.7, 10, 5.6)$ for RTILs[46] and (10, 10, 80, 0.7) for colloidal nano-particle dispersions as adequate parameters of valence p, diameter σ [nm], dielectric constant ε, and the Bjerrum length l_B [nm] at room temperature $T = 300$ K. Accordingly, we have $p^2 l_B/\sigma = 8$ (RTILs) and $p^2 l_B/\sigma = 7$ (nano-particle dispersions), and the use of eqn (7) and (13) can be justified because the relation (A25) barely holds.

Next, we evaluate a realistic range of electric field strength. At $pE\sigma = 1.5$, we have $E \approx 5.5 \times 10^7$ V m^{-1} for the RTILs (*i.e.*, $(p, \sigma) = (1,0.7)$) and $E \approx 3.8 \times 10^5$ V m^{-1} for the nano-particles (*i.e.*, $(p, \sigma) = (10,10)$). These are plausible values according to previous simulation and experimental studies as follows: molecular dynamics simulations of RTILs have revealed that $E \sim 10^7$ V m^{-1} corresponds to a boundary value beyond which RTILs are reorganized into nematic-like order and exhibit anisotropic dynamics,[47] whereas, for colloidal dispersions, a magnitude of $E \sim 10^5$ V m^{-1} is within the possible range when referring to segregation of oppositely charged colloidal particles into bands perpendicular to the direction of external AC field.[17,18]

Last, let us evaluate the electric-field-induced Kirkwood crossover densities at $pE\sigma = 1.5$. We have obtained that $\bar{\kappa}^{*}\sigma$ is equal to 1.04 ($pE\sigma = 0$) and that $\bar{\kappa}^{(*1)}\sigma \approx 0.82$ ($pE\sigma = 1.5$) when adopting the modified MSA model.[43] It follows that the Kirkwood crossover density varies from 0.30 M ($pE\sigma = 0$) to 0.19 M ($pE\sigma = 1.5$) for an RTIL (1-butyl-3-methylimidazolium bis(trifluoromethylsulfonyl)imide) diluted with propylene carbonate where we set $(p, \sigma, \varepsilon, l_B) = (1,0.4,65,0.88)$. The former density (0.30 M) agrees well with experimental and simulation results[19,20] with no electric field applied, whereas the validity of density difference (0.30–0.19 = 0.11 M) due to the external electric field needs to be assessed in future.

Conflicts of interest

There are no conflicts to declare.

Open Access Article. Published on 26 May 2022. Downloaded on 7/19/2025 4:45:38 PM.
This article is licensed under a Creative Commons Attribution-NonCommercial 3.0 Unported Licence.

Appendix A. Details on modifications of the PNP model presented in Section II

We provide the detailed formulations of the results in Section II by dividing this section into four parts: general formulation of two-component fluids (Appendix A1), two modifications of the Poisson equation (Appendix A2), formulations of stochastic currents for electric-field-driven electrolytes (Appendix A3), and outline of deriving stationary correlation functions at equal times (Appendix A4). In Appendix A1, the functional-integral representation of the Dean–Kawasaki model reveals that the Gaussian approximation of the free energy difference between non-equilibrium and equilibrium free energies yields the self-energy-modified current of each component in mixtures. In Appendix A2, we validate the approximate form (7) of interaction potential $\psi(\boldsymbol{r}, t)$ for the primitive model using the modified MSA[43] model, and also demonstrate for the modified MSA model that the finite-spread Poisson equation obtained from this expression (7) leads to the higher-order Poisson eqn (15) due to the small $k\sigma$-expansion. In Appendix A3, we show that the self-energy-modified current given by eqn (3)–(6) is obtained from combining the results in Appendix A2 and that linearization of this current corresponds to the first-order expansion of non-equilibrium chemical potential around a uniform density $\bar{n}$. Appendix A4 explains that the stationary condition (A45) imposed on a general matrix form of equal-time correlation functions yields density–density and charge–charge correlation functions given by eqn (43)–(48).

1 General formulation

Stochastic current in the Dean–Kawasaki model. The stochastic equations for the density fields $n_l(\boldsymbol{r}, t)$ (l = 1,2) have been formulated based on the Dean–Kawasaki model.[11,26] We have, according to the Dean–Kawasaki model, the conservation eqn (1) for $n_l(\boldsymbol{r}, t)$ by introducing the stochastic current $\boldsymbol{J}_l(\boldsymbol{r}, t)$: the Dean–Kawasaki model provides a general form of the stochastic current $\boldsymbol{J}_l(\boldsymbol{r}, t)$ expressed as

$$\boldsymbol{J}_l(\boldsymbol{r}, t) = -\mathcal{D}n_l(\boldsymbol{r}, t)\nabla\mu_l(\boldsymbol{r}, t) - \sqrt{2\mathcal{D}n_l(\boldsymbol{r}, t)}\zeta_l(\boldsymbol{r}, t), \tag{A1}$$

$$\mu_l(\boldsymbol{r}, t) = \frac{\delta\mathcal{A}[\boldsymbol{n}]}{\delta n_l(\boldsymbol{r}, t)}. \tag{A2}$$

We can see from eqn (A1) and (A2) that there are two features of the Dean–Kawasaki model, compared with the dynamic DFT based on the deterministic density-functional equation: (i) the deterministic current, the first term on the rhs of eqn (A1), is nonlinear with respect to $n_l(\boldsymbol{r}, t)$ in general and is determined by a constrained free energy $\mathcal{A}[\boldsymbol{n}]$, instead of the equilibrium free energy functional;[37,38] (ii) addition of the stochastic current, the second term on the rhs of eqn (A1), helps us to describe fluctuating phenomena.

Functional-integral representation of constrained free energy $\mathcal{A}[\boldsymbol{n}]$. It has been shown that the constrained free energy $\mathcal{A}[\boldsymbol{n}]$ as a functional of given density fields $\boldsymbol{n}(\boldsymbol{r}, t) = (n_1(\boldsymbol{r}, t), n_2(\boldsymbol{r}, t))^{\mathrm{T}}$ can be expressed by considering fluctuating potential fields $\boldsymbol{\phi}(\boldsymbol{r}, t) = (\phi_1(\boldsymbol{r}, t), \phi_2(\boldsymbol{r}, t))^{\mathrm{T}}$, which are conjugate to $\boldsymbol{n}(\boldsymbol{r},t)$, in addition to an adjusted potential field $\phi_l^{\mathrm{dft}}(\boldsymbol{r}, t)$ similar to that of the equilibrium DFT.[37,38] Extending the previous result[24,28] to the expression for two-component systems (see Appendix B for details), we have

$$\mathrm{e}^{-\mathcal{A}[\boldsymbol{n}]} = \prod_{l=1}^{2}\int D\phi_l\Delta[n_l]\mathrm{e}^{-F[\boldsymbol{n},\boldsymbol{\phi}]}, \tag{A3}$$

with the following constraint imposed by the canonical ensemble:

$$\Delta[n_l] = \begin{cases} 1 & \left(\int \mathrm{d}^3\boldsymbol{r}n_l(\boldsymbol{r}) = N\right) \\ 0 & \left(\int \mathrm{d}^3\boldsymbol{r}n_l(\boldsymbol{r}) \neq N\right), \end{cases} \tag{A4}$$

where the total number of either anions or cations is equally N. The free-energy functional $F[\boldsymbol{n}, \boldsymbol{\phi}]$ in the exponent of eqn (A3) is defined using the grand potential of the primitive model with an imaginary external field $i\boldsymbol{\phi}(\boldsymbol{r})$ applied, and can be divided into two parts (see Appendix B for details):

$$F[\boldsymbol{n}, \boldsymbol{\phi}] = F[\boldsymbol{n},0] + \Delta F[\boldsymbol{n}, \boldsymbol{\phi}]. \tag{A5}$$

The free-energy functional $F[\boldsymbol{n},0]$ in the absence of fluctuating potential reduces to the intrinsic Helmholtz free energy, a key thermodynamic quantity in the equilibrium DFT.[37,38] It follows that $F[\boldsymbol{n},0]$ is related to the chemical potential μ_{eq} in equilibrium through the following stationary equation:

$$\frac{\delta F[\boldsymbol{n}, 0]}{\delta n_l(\boldsymbol{r}, t)} = \mu_{\mathrm{eq}} - \varphi_l^{\mathrm{dft}}(\boldsymbol{r}, t) \equiv \mu_l^0[\boldsymbol{n}], \tag{A6}$$

where a non-equilibrium chemical potential $\mu_l^0[\boldsymbol{n}]$ is a functional of $\boldsymbol{n}(\boldsymbol{r}, t)$ because the external potential distribution $\varphi_l^{\mathrm{dft}}(\boldsymbol{r}, t)$ is adjusted to identify $n_l(\boldsymbol{r}, t)$ with the equilibrium density as is the case with the equilibrium DFT (see Appendix B for details).[37,38]

Decomposition of the stochastic current given by eqn (A1). It follows from eqn (A2)–(A6) that

$$\mu_l[\boldsymbol{n}] = \mu_l^0[\boldsymbol{n}] + \mu_l^\delta[\boldsymbol{n}] - \mu_N, \tag{A7}$$

$$\mu_l^\delta[\boldsymbol{n}] = \left\langle \frac{\delta\Delta F[\boldsymbol{n}, \boldsymbol{\phi}]}{\delta n_l(\boldsymbol{r}, t)} \right\rangle_\phi \equiv \frac{\prod_{l=1}^{2}\int D\phi_l\left(\frac{\delta\Delta F}{\delta n_l}\right)\mathrm{e}^{-\Delta F[\boldsymbol{n},\boldsymbol{\phi}]}}{\prod_{l=1}^{2}\int D\phi_l\mathrm{e}^{-\Delta F[\boldsymbol{n},\boldsymbol{\phi}]}}, \tag{A8}$$

where μ_N corresponds to the Lagrange multiplier to enforce the constraint $\Delta[n_l]$ given by eqn (A4). Correspondingly, the stochastic current $\boldsymbol{J}_l(\boldsymbol{r}, t)$ can be decomposed into three parts:

$$\boldsymbol{J}_l(\boldsymbol{r}, t) = \boldsymbol{J}_l^0(\boldsymbol{r}, t) + \boldsymbol{J}_l^\delta(\boldsymbol{r}, t) - \sqrt{2\mathcal{D}n_l(\boldsymbol{r}, t)}\zeta_l(\boldsymbol{r}, t), \tag{A9}$$

where eqn (A1), (A7) and (A8) provide

$$\boldsymbol{J}_l^0(\boldsymbol{r}, t) = -\mathcal{D}n_l(\boldsymbol{r}, t)\nabla\mu_l^0[\boldsymbol{n}], \tag{A10}$$

$$\boldsymbol{J}_l^\delta(\boldsymbol{r}, t) = -\mathcal{D}n_l(\boldsymbol{r}, t)\nabla\mu_l^\delta[\boldsymbol{n}]. \tag{A11}$$

This journal is © The Royal Society of Chemistry 2022

Open Access Article. Published on 26 May 2022. Downloaded on 7/19/2025 4:45:38 PM.
This article is licensed under a Creative Commons Attribution-NonCommercial 3.0 Unported Licence.

While the expression (116) indicates that $\boldsymbol{J}_l^0(\boldsymbol{r}, t)$ is the conventional current used in the deterministic density-functional equation, the additional current $\boldsymbol{J}_l^\delta(\boldsymbol{r}, t)$ is obtained from eqn (A2), (A7) and (A8).

Here we adopt the Ramakrishnan–Yussouf functional[38] as the equilibrium free energy $F[\boldsymbol{n}, 0]$, yielding

$$\begin{aligned}\mu_l^0[\boldsymbol{n}] &= \ln n_l(\boldsymbol{r}, t) + (-1)^{l-1} p\Psi(\boldsymbol{r}) \\ &\quad - \int \mathrm{d}^3\boldsymbol{r}' \sum_{m=1}^{2} c_{lm}(\boldsymbol{r}-\boldsymbol{r}') n_m(\boldsymbol{r}', t),\end{aligned} \tag{A12}$$

with $c_{lm}(\boldsymbol{r}-\boldsymbol{r}')$ denoting the DCF between the l-th and m-th ions. Eqn (A12) yields $\boldsymbol{J}_l^0(\boldsymbol{r}, t)$ for electric-field-driven electrolytes in the presence of an applied steady potential $\Psi(\boldsymbol{r})$ as well as the interaction potential,

$$\psi_l(\boldsymbol{r}, t) = -\int \mathrm{d}^3\boldsymbol{r}' \sum_{m=1}^{2} c_{lm}(\boldsymbol{r}-\boldsymbol{r}') n_m(\boldsymbol{r}', t), \tag{A13}$$

which is a time-varying potential due to the time dependence of $n_m(\boldsymbol{r}', t)$. Combining eqn (A10), (A12) and (A13), we have

$$\begin{aligned}\boldsymbol{J}_l^0(\boldsymbol{r}, t) &= \mathcal{D} n_l(\boldsymbol{r}, t)(-1)^{l-1} p\mathbf{E} \\ &\quad - \mathcal{D} n_l(\boldsymbol{r}, t)\nabla\{\ln n_l(\boldsymbol{r}, t) + \psi_l(\boldsymbol{r}, t)\},\end{aligned} \tag{A14}$$

where the applied electric field $\boldsymbol{E} \equiv -\nabla\Psi(\boldsymbol{r})$ generates, in units of $k_\mathrm{B}T$, an external force $(-1)^{l-1}p\boldsymbol{E}$ exerted on a cation ($l = 1$) or an anion ($l = 2$).

Self-energy contribution.[10,25] We evaluate the free-energy difference $\Delta F[\boldsymbol{n}, \boldsymbol{\phi}]$ in the Gaussian approximation, or the Gaussian expansion around the equilibrium free-energy functional $F[\boldsymbol{n}, 0]$ with the density distributions being fixed at $\boldsymbol{n}(\boldsymbol{r}, t)$. Namely, $\Delta F[\boldsymbol{n}, \boldsymbol{\phi}]$ is expressed by the quadratic term of fluctuating $\boldsymbol{\phi}$-fields:

$$\Delta F[\boldsymbol{n}, \boldsymbol{\phi}] = \frac{1}{2}\int\int \mathrm{d}^3\boldsymbol{r}\mathrm{d}^3\boldsymbol{r}' \boldsymbol{\phi}(\boldsymbol{r})^T \mathcal{N}(\boldsymbol{r}-\boldsymbol{r}')\boldsymbol{\phi}(\boldsymbol{r}'), \tag{A15}$$

where the $\mathcal{N}$-matrix is given by

$$\boldsymbol{\mathcal{N}}(\boldsymbol{r}-\boldsymbol{r}') = \begin{pmatrix} \mathcal{N}_{11}(\boldsymbol{r}-\boldsymbol{r}') & \mathcal{N}_{12}(\boldsymbol{r}-\boldsymbol{r}') \\ \mathcal{N}_{21}(\boldsymbol{r}-\boldsymbol{r}') & \mathcal{N}_{22}(\boldsymbol{r}-\boldsymbol{r}') \end{pmatrix}, \tag{A16}$$

$$\mathcal{N}_{lm}(\boldsymbol{r}-\boldsymbol{r}') = n_l(\boldsymbol{r})\{\delta_{lm}\delta(\boldsymbol{r}-\boldsymbol{r}') + h_{lm}(\boldsymbol{r}-\boldsymbol{r}')n_m(\boldsymbol{r}')\}, \tag{A17}$$

using the total correlation functions $h_{lm}(\boldsymbol{r}-\boldsymbol{r}')$ between the l-th and m-th ions. As detailed in Appendix C, combination of eqn (A8) and (A15) yields eqn (9):

$$\mu_l^\delta[\boldsymbol{n}] = \frac{u(\boldsymbol{r}, t)}{2} = \frac{1}{2}\lim_{\boldsymbol{r}\to\boldsymbol{r}'}\{c_{ll}(\boldsymbol{r}-\boldsymbol{r}') - h_{ll}(\boldsymbol{r}-\boldsymbol{r}')\}. \tag{A18}$$

It follows from eqn (A11) and (A18) that

$$\begin{aligned}\boldsymbol{J}_l^\delta(\boldsymbol{r}, t) &= -\mathcal{D} n_l(\boldsymbol{r}, t)\frac{\nabla u(\boldsymbol{r}, t)}{2} \\ &= -\mathcal{D} n_l(\boldsymbol{r}, t)\frac{\nabla c_{ll}(0)}{2},\end{aligned} \tag{A19}$$

where use has been made of the identity, $h_{ll}(0) = -1$ independent of $n_l(\boldsymbol{r}, t)$, in the last equality.

2. Modified Poisson equations given by eqn (14) and (15)

The DCF form given by eqn (12) and (13). In the modified MSA,[43] the DCF is of the following form:

$$-c_{lm}(\boldsymbol{k}) = \frac{4\pi}{\boldsymbol{k}^2} f_{lm}(\boldsymbol{k}), \tag{A20}$$

$$f_{lm}(\boldsymbol{k}) = f_{lm}^\mathrm{c}(\boldsymbol{k}) + f_{lm}^\mathrm{h}(\boldsymbol{k}), \tag{A21}$$

$$f_{lm}^\mathrm{c}(\boldsymbol{k}) = (-1)^{l+m} p^2 l_\mathrm{B} \cos(k\sigma), \tag{A22}$$

$$f_{lm}^\mathrm{h}(\boldsymbol{k}) = -\sigma\left\{\cos(k\sigma) - \frac{\sin(k\sigma)}{k\sigma}\right\}, \tag{A23}$$

where $f_{lm}(\boldsymbol{k})$ is separated into two parts, f_{lm}^c and f_{lm}^h. Eqn (A21) reduces to

$$f_{lm}(\boldsymbol{k}) \approx f_{lm}^\mathrm{c}(\boldsymbol{k}) = (-1)^{l+m} p^2 l_\mathrm{B} \cos(k\sigma) \tag{A24}$$

when

$$\frac{p^2 l_\mathrm{B}}{\sigma} \gg 1. \tag{A25}$$

Namely, the above expression of the DCF given by eqn (12) and (13) is verified in the modified MSA[43] under the condition (A25). It is noted that the approximation (A24) applies to the primitive model because $f_{lm}^\mathrm{c}(\boldsymbol{k})$ represents Coulomb interactions including steric effects.[15] The relation (A25) corresponds to the strong-coupling condition for one-component plasma, implying that the strong Coulomb interactions justify the negligibility of f_{lm}^h given by eqn (A23). In this paper, we have supposed that, in general, the simplified form (13) applies to aqueous electrolytes if only because of $p^2 l_\mathrm{B}/\sigma > 1$ (see Section V for a more detailed comparison between the relation (A25) and experimental conditions).

Finite-spread Poisson equation: derivation of eqn (14).[13,15,24,39–41] The two interaction potentials, $\psi_1(\boldsymbol{r}, t)$ and $\psi_2(\boldsymbol{r}, t)$, have been defined in eqn (A13); however, the approximate form of the DCF given by eqn (13) justifies that

$$\psi(\boldsymbol{r}, t) = \psi_1(\boldsymbol{r}, t) = -\psi_2(\boldsymbol{r}, t). \tag{A26}$$

Thus, the expression (7) of $\psi(\boldsymbol{r}, t)$ has been verified by eqn (A26), and the approximate form (13) follows the notations of

$$c_{11}(\boldsymbol{r}, t) = c_{22}(\boldsymbol{r}, t) = c(\boldsymbol{r}, t), \tag{A27}$$

$$c_{12}(\boldsymbol{r}, t) = c_{21}(\boldsymbol{r}, t) = -c(\boldsymbol{r}, t), \tag{A28}$$

thereby leading to the finite-spread Poisson eqn (14).

Higher-order Poisson equation: derivation of eqn (15).[5–10,21–24] We perform the small $k\sigma$-expansion of $\omega(\boldsymbol{k})$ in eqn (13), yielding

$$\omega(\boldsymbol{k}) \approx 1 - \frac{(k\sigma)^2}{2}, \tag{A29}$$

irrespective of the model forms given by eqn (12). It follows from eqn (7), (8), (12) and (13) that the Fourier transform of the Poisson

Open Access Article. Published on 26 May 2022. Downloaded on 7/19/2025 4:45:38 PM.
This article is licensed under a Creative Commons Attribution-NonCommercial 3.0 Unported Licence.

equation reads

$$\begin{aligned}\boldsymbol{k}^2\psi(\boldsymbol{k}) &= 4\pi p^2 l_{\mathrm{B}}\omega(-\boldsymbol{k})q(\boldsymbol{k},t)\\ &= \frac{(pe)^2}{k_{\mathrm{B}}T\varepsilon}\left\{1-\frac{(k\sigma)^2}{2}\right\}q(\boldsymbol{k},t),\end{aligned} \tag{A30}$$

which is further reduced to

$$k_{\mathrm{B}}T\varepsilon\left(1+\frac{\boldsymbol{k}^2\sigma^2}{2}\right)\boldsymbol{k}^2\psi(\boldsymbol{k}) = (pe)^2 q(\boldsymbol{k},t), \tag{A31}$$

in the small $k\sigma$-expansion: $(1-\boldsymbol{k}^2\sigma^2/2)^{-1} \approx 1+\boldsymbol{k}^2\sigma^2/2$. The real-space representation of eqn (A31) is the higher-order Poisson eqn (15).

3. Stochastic mPNP currents given by eqn (3) and (30)

Confirming the self-energy-modified PNP current given by eqn (3). Eqn (A26) reads

$$\psi_l(\boldsymbol{r}) = (-1)^{l-1}\psi(\boldsymbol{r}). \tag{A32}$$

Plugging this expression (A32) into eqn (A14), combination of eqn (A9), (A14) and (A19) provides

$$\begin{aligned}\boldsymbol{J}_l(\boldsymbol{r},t) &= \mathcal{D}n_l(\boldsymbol{r},t)(-1)^{l-1}p\boldsymbol{E}\\ &\quad-\mathcal{D}n_l(\boldsymbol{r},t)\nabla\left\{\ln n_l(\boldsymbol{r},t)+(-1)^{l-1}\psi(\boldsymbol{r},t)+\frac{u(\boldsymbol{r},t)}{2}\right\}\\ &\quad-\sqrt{2\mathcal{D}n_l(\boldsymbol{r},t)}\zeta_l(\boldsymbol{r},t).\end{aligned} \tag{A33}$$

While eqn (A18) and (A27) with the notation of $h_{ll}(\boldsymbol{r}) = h(\boldsymbol{r})$ verify the self-energy $u(\boldsymbol{r}, t)$ given by eqn (9)–(11), it has been confirmed in the preceding subsection that $\psi(\boldsymbol{r}, t)$ satisfies eqn (15). Thus, we have proved that eqn (A33) is of the same form as eqn (3) with eqn (4) and (6).

Derivation of linear mPNP current given by eqn (30).[13–15] Let $\nu_l(\boldsymbol{r}, t)$ be the density difference:

$$\nu_l(\boldsymbol{r},t) = n_l(\boldsymbol{r},t)-\bar{n}. \tag{A34}$$

To linearize the self-energy-modified current given by eqn (3), we expand the chemical potential μ_l around $n_1(\boldsymbol{r}, t) = n_2(\boldsymbol{r}, t) = \bar{n}$ (or $q \equiv 0$) to the first order in $\nu_l(\boldsymbol{r}, t)$:

$$\begin{aligned}\mu_l[\boldsymbol{n}] &= \ln n_l(\boldsymbol{r},t)+(-1)^{l-1}\psi(\boldsymbol{r},t)+\frac{u(\boldsymbol{r},t)}{2}\\ &= \mu_l[\bar{n}]+\sum_{m=1}^{2}\int \mathrm{d}^3\boldsymbol{r}'\frac{\delta\mu_l[\boldsymbol{n}]}{\delta n_m(\boldsymbol{r}',t)}\bigg|_{n_m=\bar{n}}\nu_m(\boldsymbol{r}',t)\\ &= \mu_l[\bar{n}]+\frac{\nu_l(\boldsymbol{r},t)}{\bar{n}}\\ &\quad+\sum_{m=1}^{2}\int \mathrm{d}^3\boldsymbol{r}'\frac{\delta U_l[\boldsymbol{n}]}{\delta n_m(\boldsymbol{r}',t)}\bigg|_{n_m=\bar{n}}\nu_m(\boldsymbol{r}',t),\end{aligned} \tag{A35}$$

with $\mu_l[\bar{n}]$ denoting $\mu_l[\bar{n}] = \mu_l[(\bar{n}, \bar{n})^{\mathrm{T}}]$. Since we have

$$\begin{aligned}&\sum_{m=1}^{2}\int \mathrm{d}^3\boldsymbol{r}'\frac{\delta U_l[\boldsymbol{n}]}{\delta n_m(\boldsymbol{r}',t)}\bigg|_{n_m=\bar{n}}\nu_m(\boldsymbol{r}',t)\\ &\quad= -(-1)^{l-1}\int \mathrm{d}\boldsymbol{r}'c(\boldsymbol{r}-\boldsymbol{r}')q(\boldsymbol{r}',t)\\ &\quad= (-1)^{l-1}\psi(\boldsymbol{r},t),\end{aligned} \tag{A36}$$

neglecting the contribution from the triplet DCF, eqn (A35) simply reads

$$\mu_l[\boldsymbol{n}] = \mu_l[\bar{n}]+\frac{\nu_l(\boldsymbol{r},t)}{\bar{n}}+-(-1)^{l-1}\psi(\boldsymbol{r},t) \tag{A37}$$

Combining eqn (3) and (A37), the mPNP current becomes, to the lowest order,

$$\begin{aligned}\begin{pmatrix}\boldsymbol{J}_1\\ \boldsymbol{J}_2\end{pmatrix} &= -\mathcal{D}\begin{pmatrix}\nabla\nu_1(\boldsymbol{r},t)+\bar{n}\nabla\psi(\boldsymbol{r},t)-n_1(\boldsymbol{r},t)p\boldsymbol{E}\\ \nabla\nu_2(\boldsymbol{r},t)-\bar{n}\nabla\psi(\boldsymbol{r},t)+n_2(\boldsymbol{r},t)p\boldsymbol{E}\end{pmatrix}\\ &\quad-\sqrt{2\mathcal{D}\bar{n}}\begin{pmatrix}\zeta_1(\boldsymbol{r},t)\\ \zeta_2(\boldsymbol{r},t)\end{pmatrix}.\end{aligned} \tag{A38}$$

We also note that

$$\nabla\rho(\boldsymbol{r},t) = \nabla\{\nu_1(\boldsymbol{r},t)+\nu_2(\boldsymbol{r},t)\}, \tag{A39}$$

$$\nabla q(\boldsymbol{r},t) = \nabla\{\nu_1(\boldsymbol{r},t)-\nu_2(\boldsymbol{r},t)\}. \tag{A40}$$

Thus, eqn (A38)–(A40) lead to the stochastic currents, $\boldsymbol{J}_\rho = \boldsymbol{J}_1+\boldsymbol{J}_2$ and $\boldsymbol{J}_q = \boldsymbol{J}_1-\boldsymbol{J}_2$, given by eqn (30).

4 Equal-time correlation functions given by eqn (43)–(46)

Stationary condition of equal-time correlation matrix. The compact form (32) of the stochastic equation is solved to obtain[13,15]

$$\boldsymbol{\theta}(\boldsymbol{k},t) = \left\{\int_{-\infty}^{t}\mathrm{d}s\mathrm{e}^{-\mathcal{D}\mathcal{K}(\boldsymbol{k})(t-s)}\right\}\sqrt{4\mathcal{D}\bar{n}}\boldsymbol{\eta}(\boldsymbol{k}). \tag{A41}$$

It follows from eqn (5) and (29) that

$$\left\langle\boldsymbol{\eta}(\boldsymbol{k},t)\boldsymbol{\eta}(-\boldsymbol{k},t)^{\mathrm{T}}\right\rangle = (2\pi)^3\begin{pmatrix}\boldsymbol{k}^2\delta(t-t') & 0\\ 0 & \boldsymbol{k}^2\delta(t-t')\end{pmatrix}. \tag{A42}$$

Plugging eqn (A41) and (A42) into the definition (40) of the equal-time correlation matrix, we have

$$\mathcal{C}(\boldsymbol{k},t) = \iint_{-\infty}\mathrm{d}s\mathrm{d}s'\mathrm{e}^{-\mathcal{D}\mathcal{K}(t-s)}\mathcal{D}\mathcal{R}\mathrm{e}^{-\mathcal{D}\mathcal{K}^{\dagger}(t-s')}, \tag{149}$$

where the relation (A42) generates the following matrix:

$$\mathcal{R}(\boldsymbol{k}) = (2\pi)^3\begin{pmatrix}4\bar{n}\boldsymbol{k}^2 & 0\\ 0 & 4\bar{n}\boldsymbol{k}^2\end{pmatrix}. \tag{A44}$$

It has been shown that the stationary condition $\mathrm{d}\mathcal{C}(\boldsymbol{k}, t)/\mathrm{d}t = 0$ for the expression (A43) reads[13,15]

$$\mathcal{K}\mathcal{C}+\mathcal{C}\mathcal{K}^{\dagger} = \mathcal{R}. \tag{A45}$$

The four matrix elements of $\mathcal{C}$, or the four kinds of correlation functions in eqn (40), can be determined by four simultaneous equations arising from the above stationary condition (A45) (see Appendix D for details).

This journal is © The Royal Society of Chemistry 2022

Open Access Article. Published on 26 May 2022. Downloaded on 7/19/2025 4:45:38 PM.
This article is licensed under a Creative Commons Attribution-NonCommercial 3.0 Unported Licence.

Density–density and charge–charge correlation functions at equal times: derivation scheme of eqn (43)–(48). We are concerned with the stationary density–density and charge–charge correlation functions at equal times, $\mathcal{C}^{\rm st}_{\rho\rho}$ and $\mathcal{C}^{\rm st}_{qq}$, among the matrix elements of $\mathcal{C}$. As detailed in Appendix D, the solution to eqn (A45) reads

$$\mathcal{P}(\boldsymbol{k})\begin{pmatrix}\mathcal{C}^{\rm st}_{\rho\rho}(\boldsymbol{k})\\ \mathcal{C}^{\rm st}_{qq}(\boldsymbol{k})\end{pmatrix}=(2\pi)^3\mathcal{G}_2(\boldsymbol{k})\begin{pmatrix}2\overline{n}\boldsymbol{k}^2\\ 2\overline{n}\boldsymbol{k}^2\end{pmatrix}, \tag{A46}$$

where $\mathcal{G}_2(\boldsymbol{k})$ has been defined in eqn (45), and the matrix elements of $\mathcal{P}(\boldsymbol{k})$ is given by

$$\mathcal{P}(\boldsymbol{k})=\begin{pmatrix}\boldsymbol{k}^2\mathcal{G}_2(\boldsymbol{k})+k_x^2(pE)^2 & -k_x^2(pE)^2\\ -k_x^2(pE)^2 & \mathcal{G}_1(\boldsymbol{k})\mathcal{G}_2(\boldsymbol{k})+k_x^2(pE)^2\end{pmatrix}. \tag{A47}$$

Obviously, eqn (A46) and (A47) transform to eqn (43)–(48).

Appendix B. Details on the constrained free energy $\mathcal{A}[\boldsymbol{n}]$ of a given density distribution $n(r, t)$

We consider the overdamped dynamics of ions with the total number N of charged spheres being fixed. Hence, the constrained free-energy functional $\mathcal{A}[\boldsymbol{n}]$ of a given density distribution $n_l(\boldsymbol{r}, t)$ (l = 1,2) is defined for the canonical ensemble using the contour integral over a complex variable $w = e^{\mu}$:[28]

$$\begin{aligned}e^{-\mathcal{A}[\boldsymbol{n}]} &= \left(\frac{1}{2\pi i}\oint\frac{dw}{w^{N+1}}\right)^2\\ &\times\left(\mathrm{Tr}e^{-U[\hat{\boldsymbol{n}}]}\prod_{l=1}^{2}\prod_{\boldsymbol{r}}\delta[\widehat{n}_l(\boldsymbol{r},t)-n_l(\boldsymbol{r},t)]\right),\end{aligned} \tag{B1}$$

$$\mathrm{Tr}=\left(\sum_{N=0}^{\infty}\frac{1}{N!}\right)^2\prod_{l=1}^{2}\int d\boldsymbol{r}_1^l\cdots\int d\boldsymbol{r}_N^l, \tag{B2}$$

$$\begin{aligned}U[\hat{\boldsymbol{n}}] &= \sum_{l=1}^{2}\sum_{m=1}^{2}\left[\frac{1}{2}\iint d^3\boldsymbol{r}d^3\boldsymbol{r}'\widehat{n}_l(\boldsymbol{r})v_{lm}(\boldsymbol{r}-\boldsymbol{r}')\widehat{n}_m(\boldsymbol{r})\right.\\ &\left.-\int d^3\boldsymbol{r}\widehat{n}_l(\boldsymbol{r})\mu\right].\end{aligned} \tag{B3}$$

In eqn (B1), the Dirac delta functional represents the constraint on the original density distribution $\widehat{n}_l(\boldsymbol{r})=\sum_{i=1}^{N}\delta[\boldsymbol{r}-\boldsymbol{r}_i^l(t)]$. It has been shown for one-component fluid that the constrained free energy functional is expressed by the functional integral over a fluctuating potential field. Similarly, we have

$$\begin{aligned}e^{-\mathcal{A}[\boldsymbol{n}]} &= \left(\frac{1}{2\pi i}\oint\frac{dw}{w^{N+1}}\right)^2\prod_{l=1}^{2}\int D\phi_l e^{-F[\boldsymbol{n},\boldsymbol{\phi}]+\int d^3\boldsymbol{r}n_l(\boldsymbol{r})\mu}\\ &= \prod_{l=1}^{2}\int D\phi_l\Delta[n_l]e^{-F[\boldsymbol{n},\boldsymbol{\phi}]},\end{aligned} \tag{B4}$$

where

$$\begin{aligned}&F[\boldsymbol{n},\boldsymbol{\phi}]-\sum_{l=1}^{2}\int d\boldsymbol{r}n_l(\boldsymbol{r})\mu\\ &=\Omega[\boldsymbol{\varphi}^{\rm dft}-i\boldsymbol{\phi}]-\sum_{l=1}^{2}\int d\boldsymbol{r}n_l(\boldsymbol{r})\left\{\varphi_l^{\rm dft}(\boldsymbol{r})-i\phi_l(\boldsymbol{r})\right\},\end{aligned} \tag{B5}$$

and the superscript "dft" denotes the equilibrium DFT[37] according to which the external field $\varphi_l^{\rm dft}(\boldsymbol{r})$ is used for ensuring that the equilibrium density found from the grand potential $\Omega[\boldsymbol{\varphi}]$ is equated with $n_l(\boldsymbol{r})$:

$$\left.\frac{\delta\Omega[\boldsymbol{\varphi}]}{\delta\varphi_l(\boldsymbol{r})}\right|_{\varphi_l=\varphi_l^{\rm dft}}=n_l(\boldsymbol{r}). \tag{B6}$$

The free-energy functional $F[\boldsymbol{n}, 0]$ in the absence of fluctuating $\boldsymbol{\phi}$-field corresponds to the intrinsic Helmholtz free energy that is related to the grand potential $\Omega[\boldsymbol{\varphi}^{\rm dft}]$ through the Legendre transform using the external field $\varphi_l^{\rm dft}(\boldsymbol{r})$:

$$F[\boldsymbol{n},0]-\sum_{l=1}^{2}\int d\boldsymbol{r}n_l(\boldsymbol{r})\mu=\Omega[\boldsymbol{\varphi}^{\rm dft}]-\sum_{l=1}^{2}\int d\boldsymbol{r}n_l(\boldsymbol{r})\varphi_l^{\rm dft}(\boldsymbol{r}), \tag{B7}$$

as well as the equilibrium DFT.

Appendix C. Derivation of μ_l^{δ} given by eqn (A18)

Let us introduce the potential–potential correlation matrix $\boldsymbol{\Phi}$ that represents the set of potential–potential correlation functions defined by

$$\Phi(\boldsymbol{r}-\boldsymbol{r}')=\left\langle\boldsymbol{\phi}(\boldsymbol{r})\boldsymbol{\phi}^{\rm T}(\boldsymbol{r}')\right\rangle_{\phi} \tag{C1}$$

$$=\begin{pmatrix}\langle\Phi_{11}(\boldsymbol{r}-\boldsymbol{r}')\rangle_{\phi} & \langle\Phi_{12}(\boldsymbol{r}-\boldsymbol{r}')\rangle_{\phi}\\ \langle\Phi_{21}(\boldsymbol{r}-\boldsymbol{r}')\rangle_{\phi} & \langle\Phi_{22}(\boldsymbol{r}-\boldsymbol{r}')\rangle_{\phi}\end{pmatrix}, \tag{C2}$$

where $\langle\Phi_{lm}(\boldsymbol{r}-\boldsymbol{r}')\rangle_{\phi}$ is related to the DCF function $c_{lm}(\boldsymbol{r}-\boldsymbol{r}')$ as

$$\begin{aligned}\langle\Phi_{lm}(\boldsymbol{r}-\boldsymbol{r}')\rangle_{\phi} &= \langle\phi_l(\boldsymbol{r})\phi_m(\boldsymbol{r}')\rangle_{\phi}\\ &= \frac{\delta_{lm}\delta(\boldsymbol{r}-\boldsymbol{r}')}{n_l(\boldsymbol{r})}-c_{lm}(\boldsymbol{r}-\boldsymbol{r}').\end{aligned} \tag{C3}$$

The average, $\langle\phi_l(\boldsymbol{r})\phi_m(\boldsymbol{r}')\rangle_{\phi}$, has been performed over the fluctuating potential field as

$$\langle\phi_l(\boldsymbol{r})\phi_m(\boldsymbol{r}')\rangle_{\phi}=\frac{\prod_{l=1}^{2}\int D\phi_l\phi_l(\boldsymbol{r})\phi_m(\boldsymbol{r}')e^{-\Delta F[\boldsymbol{n},\boldsymbol{\phi}]}}{\prod_{l=1}^{2}\int D\phi_l e^{-\Delta F[\boldsymbol{n},\boldsymbol{\phi}]}}, \tag{C4}$$

following the expression (A8). Hence, eqn (C4) yields eqn (C3) as far as the Gaussian functional form (A15) for $\Delta F[\boldsymbol{n}, \boldsymbol{\phi}]$ is concerned. It is found from eqn (A17) and (C3) that the Ornstein–Zernike equations for two-component

Open Access Article. Published on 26 May 2022. Downloaded on 7/19/2025 4:45:38 PM.
This article is licensed under a Creative Commons Attribution-NonCommercial 3.0 Unported Licence.

liquids read

$$\boldsymbol{\mathcal{N}}(\boldsymbol{k})\boldsymbol{\Phi}(-\boldsymbol{k}) = \boldsymbol{I}, \tag{C5}$$

indicating that the Fourier-transformed matrix $\boldsymbol{\Phi}(-\boldsymbol{k})$ is the inverse of density–density correlation matrix $\boldsymbol{\mathcal{N}}(\boldsymbol{k})$.

Considering that $\mathcal{N}_{12} = \mathcal{N}_{21}$ for the density–density correlation function $\mathcal{N}_{lm}(\boldsymbol{r}-\boldsymbol{r}')$ defined by eqn (A17), eqn (A15) leads to

$$\left\langle \frac{\delta \Delta F[\boldsymbol{n},\boldsymbol{\phi}]}{\delta n_1(\boldsymbol{r})} \right\rangle_\phi = \left\langle \frac{\delta}{\delta n_1(\boldsymbol{r})} \iint \mathrm{d}^3\boldsymbol{r}\mathrm{d}^3\boldsymbol{r}' \frac{1}{2}\mathcal{N}_{11}(\boldsymbol{r}-\boldsymbol{r}')\Phi_{11}(\boldsymbol{r}-\boldsymbol{r}') \right\rangle_\phi + \left\langle \frac{\delta}{\delta n_1(\boldsymbol{r})} \iint \mathrm{d}^3\boldsymbol{r}\mathrm{d}^3\boldsymbol{r}' \mathcal{N}_{12}(\boldsymbol{r}-\boldsymbol{r}')\Phi_{12}(\boldsymbol{r}-\boldsymbol{r}') \right\rangle_\phi . \tag{C6}$$

To evaluate the above functional derivatives, we introduce the following notations: it follows from eqn (A17) that

$$\begin{aligned} &\frac{\delta}{\delta n_l(\boldsymbol{r})} \iint \mathrm{d}^3\boldsymbol{r}\mathrm{d}^3\boldsymbol{r}' \mathcal{N}_{lm}(\boldsymbol{r}-\boldsymbol{r}') = \int \mathrm{d}^3\boldsymbol{r}' \mathcal{N}^{(1)}_{lm}(\boldsymbol{r}-\boldsymbol{r}'), \\ &\mathcal{N}^{(1)}_{lm} = \delta_{lm}\{\delta(\boldsymbol{r}-\boldsymbol{r}') + h_{lm}(\boldsymbol{r}-\boldsymbol{r}')n_m(\boldsymbol{r}')\} \\ &\mathcal{N}^{(1)}_{lm} = \delta_{lm}\{\delta(\boldsymbol{r}-\boldsymbol{r}') + h_{lm}(\boldsymbol{r}-\boldsymbol{r}')n_m(\boldsymbol{r}'), \end{aligned} \tag{C7}$$

with which we have

$$\begin{aligned} &\left\langle \frac{\delta}{\delta n_l(\boldsymbol{r})} \iint \mathrm{d}^3\boldsymbol{r}\mathrm{d}^3\boldsymbol{r}' \mathcal{N}_{lm}(\boldsymbol{r}-\boldsymbol{r}')\Phi_{lm}(\boldsymbol{r}-\boldsymbol{r}') \right\rangle_\phi \\ &= \frac{\prod_{l=1}^{2} \int D\phi_l \mathrm{e}^{-\Delta F[\boldsymbol{n},\boldsymbol{\phi}]} \left[\frac{\delta}{\delta n_l(\boldsymbol{r})} \iint \mathrm{d}^3\boldsymbol{r}\mathrm{d}^3\boldsymbol{r}' \mathcal{N}_{lm}\Phi_{lm} \right]}{\prod_{l=1}^{2} \int D\phi_l \mathrm{e}^{-\Delta F[\boldsymbol{n},\boldsymbol{\phi}]}} \\ &= \int \mathrm{d}^3\boldsymbol{r}' \left(\mathcal{N}^{(1)}_{lm} \langle \Phi_{lm} \rangle_\phi + \mathcal{N}_{lm} \left\langle \Phi^{(1)}_{lm} \right\rangle_\phi \right), \end{aligned} \tag{C8}$$

using $\Phi^{(1)}_{lm}$, a derivative of Φ_{lm}, defined by eqn (C7) and (C8). At the same time, it is also useful to consider the following functional derivative:

$$\begin{aligned} \int \mathrm{d}^3\boldsymbol{r}' \langle \Phi_{lm} \rangle^{(1)}_\phi &= \frac{\delta}{\delta n_l(\boldsymbol{r})} \left(\iint \mathrm{d}^3\boldsymbol{r}\mathrm{d}^3\boldsymbol{r}' \langle \Phi_{lm} \rangle_\phi \right) \\ &= \frac{\delta}{\delta n_l(\boldsymbol{r})} \left\{ \frac{\delta_{lm}\delta(\boldsymbol{r}-\boldsymbol{r}')}{n_l(\boldsymbol{r})} - c_{lm}(\boldsymbol{r}-\boldsymbol{r}') \right\} \\ &= -\frac{\delta_{lm}\delta(\boldsymbol{r}-\boldsymbol{r}')}{n_l^2(\boldsymbol{r})}, \end{aligned} \tag{C9}$$

where use has been made of the expression (C3) in the last two equalities.

The unknown functional $\langle \Phi^{(1)}_{lm} \rangle_\phi$ is related to $\langle \Phi_{lm} \rangle^{(1)}_\phi$, given by eqn (C9), as

$$\begin{aligned} \int \mathrm{d}^3\boldsymbol{r}' \langle \Phi_{lm} \rangle^{(1)}_\phi &= \frac{\delta}{\delta n_l(\boldsymbol{r})} \left(\iint \mathrm{d}^3\boldsymbol{r}\mathrm{d}^3\boldsymbol{r}' \langle \Phi_{lm} \rangle_\phi \right) \\ &= \frac{\delta}{\delta n_l(\boldsymbol{r})} \left\{ \frac{\iint \mathrm{d}^3\boldsymbol{r}\mathrm{d}^3\boldsymbol{r}' \prod_{l=1}^{2} \int D\phi_l \Phi_{lm} \mathrm{e}^{-\Delta F[\boldsymbol{n},\boldsymbol{\phi}]}}{\prod_{l=1}^{2} \int D\phi_l \mathrm{e}^{-\Delta F[\boldsymbol{n},\boldsymbol{\phi}]}} \right\} \\ &= \int \mathrm{d}^3\boldsymbol{r}' \left[\left\langle \Phi^{(1)}_{lm} \right\rangle_\phi - \left\langle \Phi_{lm} \frac{\delta \Delta F[\boldsymbol{n},\boldsymbol{\phi}]}{\delta n_l(\boldsymbol{r})} \right\rangle_\phi \right. \\ &\quad \left. \times \int \mathrm{d}^3\boldsymbol{r}' \left[\left\langle \Phi^{(1)}_{lm} \right\rangle_\phi + \langle \Phi_{lm} \rangle_\phi \left\langle \frac{\delta \Delta F[\boldsymbol{n},\boldsymbol{\phi}]}{\delta n_l(\boldsymbol{r})} \right\rangle_\phi \right] \right. \\ &\approx \int \mathrm{d}^3\boldsymbol{r}' \left\langle \Phi^{(1)}_{lm} \right\rangle_\phi , \end{aligned} \tag{C10}$$

stating that $\langle \Phi^{(1)}_{lm} \rangle_\phi$ can be equated with $\langle \Phi_{lm} \rangle^{(1)}_\phi$ in the approximation of $\langle AB \rangle_\phi \approx \langle A \rangle_\phi \langle B \rangle_\phi$ for $A = \Phi_{lm}$ and $B = \delta \Delta F[\boldsymbol{n},\boldsymbol{\phi}]/\delta n_l(\boldsymbol{r})$. Thus, we obtain

$$\begin{aligned} \int \mathrm{d}^3\boldsymbol{r}' \mathcal{N}_{lm} \left\langle \Phi^{(1)}_{lm} \right\rangle &= \int \mathrm{d}^3\boldsymbol{r}' n_l(\boldsymbol{r}) \{\delta_{lm}\delta(\boldsymbol{r}-\boldsymbol{r}') + h_{lm}(\boldsymbol{r}-\boldsymbol{r}')n_m(\boldsymbol{r}')\} \\ &\quad \times \left\{ -\frac{\delta_{lm}\delta(\boldsymbol{r}-\boldsymbol{r}')}{n_l^2(\boldsymbol{r})} \right\} = -\delta_{lm} \left\{ \frac{1}{n_l(\boldsymbol{r})} + h_{lm}(0) \right\}, \end{aligned} \tag{C11}$$

from plugging eqn (C9) and (C10) into the second term in the last line of eqn (C8).

Meanwhile, we have

$$\begin{aligned} \int \mathrm{d}^3\boldsymbol{r}' \mathcal{N}^{(1)}_{lm} \langle \Phi_{lm} \rangle_\phi &= \int \mathrm{d}^3\boldsymbol{r}' [\delta_{lm}\{\delta(\boldsymbol{r}-\boldsymbol{r}') + h_{lm}(\boldsymbol{r}-\boldsymbol{r}')n_m(\boldsymbol{r}')\} \\ &\quad + h_{lm}(\boldsymbol{r}-\boldsymbol{r}')n_m(\boldsymbol{r}')] \left\{ \frac{\delta_{lm}\delta(\boldsymbol{r}-\boldsymbol{r}')}{n_l(\mathbf{r})} - c_{lm}(\boldsymbol{r}-\boldsymbol{r}') \right\}. \end{aligned} \tag{C12}$$

Hence, the combination of eqn (C11) and (C12) gives

$$\begin{aligned} &\frac{1}{2} \int \mathrm{d}^3\boldsymbol{r}' \left(\mathcal{N}^{(1)}_{11} \langle \Phi_{11} \rangle_\phi + \mathcal{N}_{11} \langle \Phi_{11} \rangle^{(1)}_\phi \right) \\ &= \frac{1}{2} \left[\frac{1}{n_1(\boldsymbol{r})} + 2h_{11}(0) - c_{11}(0) \right. \\ &\quad - 2 \int \mathrm{d}^3\boldsymbol{r}' h_{11}(\boldsymbol{r}-\boldsymbol{r}')n_1(\boldsymbol{r}')c_{11}(\boldsymbol{r}-\boldsymbol{r}') \\ &\quad \left. - \left\{ \frac{1}{n_1(\boldsymbol{r})} + h_{11}(0) \right\} \right] \\ &= \frac{1}{2}\{h_{11}(0) - c_{11}(0)\} \\ &\quad - \int \mathrm{d}^3\boldsymbol{r}' h_{11}(\boldsymbol{r}-\boldsymbol{r}')n_1(\boldsymbol{r}')c_{11}(\boldsymbol{r}-\boldsymbol{r}'), \end{aligned} \tag{C13}$$

This journal is © The Royal Society of Chemistry 2022

Open Access Article. Published on 26 May 2022. Downloaded on 7/19/2025 4:45:38 PM.
This article is licensed under a Creative Commons Attribution-NonCommercial 3.0 Unported Licence.

and

$$\begin{aligned}&\int d^3\boldsymbol{r}'\left(\mathcal{N}_{12}^{(1)}\langle\Phi_{12}\rangle_{\phi}+\mathcal{N}_{12}\langle\Phi_{12}\rangle_{\phi}^{(1)}\right)\\&=-\int d^3\boldsymbol{r}'h_{12}(\boldsymbol{r}-\boldsymbol{r}')n_2(\boldsymbol{r}')c_{12}(\boldsymbol{r}-\boldsymbol{r}').\end{aligned}\tag{C14}$$

Considering the Ornstein–Zernike equation,

$$h_{11}(0)=c_{11}(0)+\sum_{m=1}^{2}\int d^3\boldsymbol{r}'h_{1m}(\boldsymbol{r}-\boldsymbol{r}')n_m(\boldsymbol{r}')c_{1m}(\boldsymbol{r}-\boldsymbol{r}'),\tag{C15}$$

the sum of eqn (C13) and (C14) leads to

$$\begin{aligned}\frac{\overline{\delta\Delta F[\boldsymbol{n},\boldsymbol{\phi}]}}{\delta n_1(\boldsymbol{r})}&=\frac{1}{2}\{h_{11}(0)-c_{11}(0)\}\\&-\int d^3\boldsymbol{r}'h_{11}(\boldsymbol{r}-\boldsymbol{r}')n_1(\mathbf{r}')c_{11}(\boldsymbol{r}-\boldsymbol{r}')\\&-\int d^3\boldsymbol{r}'h_{12}(\boldsymbol{r}-\boldsymbol{r}')n_2(\boldsymbol{r}')c_{12}(\boldsymbol{r}-\boldsymbol{r}')\\&=\frac{1}{2}\{c_{11}(0)-h_{11}(0)\}.\end{aligned}\tag{C16}$$

Thus, the resulting form (A18) of μ_l^{δ} has been verified.

Appendix D. Solving the steady-state eqn (A45)

1. Derivation of eqn (A46) and (A47)

We calculate the matrix elements of $\mathcal{K}\mathcal{C}$ and $\mathcal{C}\mathcal{K}^{\dagger}$, using a simplified form of

$$\mathcal{K}(\boldsymbol{k})=\begin{pmatrix}\alpha & i\gamma\\ i\gamma & \alpha+\beta\end{pmatrix},\tag{D1}$$

with $\alpha=\boldsymbol{k}^2$, $\beta=\overline{\kappa}^2\omega(\boldsymbol{k})$ and $\gamma=k_xpE$. It follows that

$$\mathcal{K}\mathcal{C}=\begin{pmatrix}\alpha\mathcal{C}_{\rho\rho}^{\mathrm{st}}+i\gamma\mathcal{C}_{\rho q}^{\mathrm{st}} & \alpha\mathcal{C}_{q\rho}^{\mathrm{st}}+i\gamma\mathcal{C}_{qq}^{\mathrm{st}}\\ (\alpha+\beta)\mathcal{C}_{\rho q}^{\mathrm{st}}+i\gamma\mathcal{C}_{\rho\rho}^{\mathrm{st}} & (\alpha+\beta)\mathcal{C}_{qq}^{\mathrm{st}}+i\gamma\mathcal{C}_{q\rho}^{\mathrm{st}}\end{pmatrix},\tag{D2}$$

$$\mathcal{C}\mathcal{K}^{\dagger}=\begin{pmatrix}\alpha\mathcal{C}_{\rho\rho}^{\mathrm{st}}-i\gamma\mathcal{C}_{q\rho}^{\mathrm{st}} & (\alpha+\beta)\mathcal{C}_{q\rho}^{\mathrm{st}}-i\gamma\mathcal{C}_{\rho\rho}^{\mathrm{st}}\\ \alpha\mathcal{C}_{\rho q}^{\mathrm{st}}-i\gamma\mathcal{C}_{qq}^{\mathrm{st}} & (\alpha+\beta)\mathcal{C}_{qq}^{\mathrm{st}}-i\gamma\mathcal{C}_{\rho q}^{\mathrm{st}}\end{pmatrix}.\tag{D3}$$

The sum of eqn (D2) and (D3) provides the steady-state eqn (A45) which consists of the four kinds of equations for correlation functions as follows:

$$\begin{cases}2\alpha\mathcal{C}_{\rho\rho}^{\mathrm{st}}+i\gamma\left(\mathcal{C}_{\rho q}^{\mathrm{st}}-\mathcal{C}_{q\rho}^{\mathrm{st}}\right)=(2\pi)^3 4\overline{n}\boldsymbol{k}^2\\ 2(\alpha+\beta)\mathcal{C}_{qq}^{\mathrm{st}}-i\gamma\left(\mathcal{C}_{\rho q}^{\mathrm{st}}-\mathcal{C}_{q\rho}^{\mathrm{st}}\right)=(2\pi)^3 4\overline{n}\boldsymbol{k}^2\\ (2\alpha+\beta)\mathcal{C}_{q\rho}^{\mathrm{st}}+i\gamma\left(\mathcal{C}_{qq}^{\mathrm{st}}-\mathcal{C}_{\rho\rho}^{\mathrm{st}}\right)=0\\ (2\alpha+\beta)\mathcal{C}_{\rho q}^{\mathrm{st}}-i\gamma\left(\mathcal{C}_{qq}^{\mathrm{st}}-\mathcal{C}_{\rho\rho}^{\mathrm{st}}\right)=0.\end{cases}\tag{D4}$$

It is easy to find from the last two equations of the above set that $\mathcal{C}_{\rho q}^{\mathrm{st}}=-\mathcal{C}_{q\rho}^{\mathrm{st}}$ and

$$\mathcal{C}_{\rho q}^{\mathrm{st}}-\mathcal{C}_{q\rho}^{\mathrm{st}}=\frac{2i\gamma}{2\alpha+\beta}\left(\mathcal{C}_{qq}^{\mathrm{st}}-\mathcal{C}_{\rho\rho}^{\mathrm{st}}\right).\tag{D5}$$

Substituting eqn (D5) into the first two equations of eqn (D4), we have

$$\begin{cases}\alpha\mathcal{C}_{\rho\rho}^{\mathrm{st}}-\dfrac{\gamma^2}{2\alpha+\beta}\left(\mathcal{C}_{qq}^{\mathrm{st}}-\mathcal{C}_{\rho\rho}^{\mathrm{st}}\right)=(2\pi)^3 2\overline{n}\boldsymbol{k}^2\\ (\alpha+\beta)\mathcal{C}_{qq}^{\mathrm{st}}+\dfrac{\gamma^2}{2\alpha+\beta}\left(\mathcal{C}_{qq}^{\mathrm{st}}-\mathcal{C}_{\rho\rho}^{\mathrm{st}}\right)=(2\pi)^3 2\overline{n}\boldsymbol{k}^2,\end{cases}\tag{D6}$$

which reads

$$\frac{1}{2\alpha+\beta}\mathcal{P}(\boldsymbol{k})\begin{pmatrix}\mathcal{C}_{\rho\rho}^{\mathrm{st}}\\ \mathcal{C}_{qq}^{\mathrm{st}}\end{pmatrix}=(2\pi)^3 2\overline{n}\begin{pmatrix}\boldsymbol{k}^2\\ \boldsymbol{k}^2\end{pmatrix},\tag{D7}$$

and

$$\mathcal{P}(\boldsymbol{k})=\begin{pmatrix}\alpha(2\alpha+\beta)+\gamma^2 & -\gamma^2\\ -\gamma^2 & (\alpha+\beta)(2\alpha+\beta)+\gamma^2\end{pmatrix}.\tag{D8}$$

In the matrix elements, we note that $2\alpha+\beta=\mathcal{G}_2(\boldsymbol{k})$ and $\alpha+\beta=\mathcal{G}_1(\boldsymbol{k})$. Hence, the above expressions (D7) and (D8) are found to be equivalent to eqn (A46) and (A47).

2 Derivation of eqn (49)

Eqn (43)–(46) are combined into a single form,

$$\begin{aligned}\frac{1}{(2\pi)^3}\begin{pmatrix}\mathcal{C}_{\rho\rho}^{\mathrm{st}}(\boldsymbol{k})\\ \mathcal{C}_{qq}^{\mathrm{st}}(\boldsymbol{k})\end{pmatrix}&=\frac{2\overline{n}\boldsymbol{k}^2}{\mathcal{G}_2(\boldsymbol{k})\{\boldsymbol{k}^2\mathcal{G}_1(\boldsymbol{k})+k_x^2(pE)^2\}}\\&\times\begin{pmatrix}\mathcal{G}_1(\boldsymbol{k})\mathcal{G}_2(\boldsymbol{k})+2k_x^2(pE)^2\\ \boldsymbol{k}^2\mathcal{G}_2(\boldsymbol{k})+2k_x^2(pE)^2\end{pmatrix}.\end{aligned}\tag{D9}$$

The three propagators, $\mathcal{G}_1(\boldsymbol{k})$, $\mathcal{G}_2(\boldsymbol{k})$ and $\overline{\kappa}^2+2k_x^2(pE\overline{\kappa}^{-1})^2$, can be simply approximated by $\overline{\kappa}^2$ when considering the small wavevector region of $k_x\overline{\kappa}^{-1}\ll 1$ at a moderate field strength of $pE\overline{\kappa}^{-1}\sim 1$. This approximation allows eqn (D9) to be reduced to

$$\begin{aligned}\frac{1}{(2\pi)^3}\begin{pmatrix}\mathcal{C}_{\rho\rho}^{\mathrm{st}}(\boldsymbol{k})\\ \mathcal{C}_{qq}^{\mathrm{st}}(\boldsymbol{k})\end{pmatrix}&\approx\frac{2\overline{n}\boldsymbol{k}^2}{\overline{\kappa}^2\{\boldsymbol{k}^2+k_x^2(pE\overline{\kappa}^{-1})^2\}}\\&\times\begin{pmatrix}\overline{\kappa}^2\\ \boldsymbol{k}^2+2k_x^2(pE\overline{\kappa}^{-1})^2\end{pmatrix},\end{aligned}\tag{D10}$$

whose rearrangement leads to eqn (49).

Appendix E. Derivation of eqn (89) and (90)

The discriminant analysis of eqn (87) provides the determining equation for the Debye–Hückel length $\overline{\kappa}^{(*1)}$ on the Kirkwood

Open Access Article. Published on 26 May 2022. Downloaded on 7/19/2025 4:45:38 PM.
This article is licensed under a Creative Commons Attribution-NonCommercial 3.0 Unported Licence.

crossover:

$$\left\{1-\alpha_1\left(\overline{\kappa}^{(*1)}\right)^2\sigma^2\right\}^2 - 4\alpha_2\left(\overline{\kappa}^{(*1)}\right)^2\sigma^2\left\{\left(\overline{\kappa}^{(*1)}\right)^2\sigma^2+\mathcal{E}^2\right\}=0, \tag{E1}$$

with $\mathcal{E}^2 \equiv (pE)^2\sigma^2$. Eqn (87) reads the following quadratic equation,

$$\left(\alpha_1^2-4\alpha_2\right)X^2-2\left(\alpha_1+2\alpha_2\mathcal{E}^2\right)X+1=0, \tag{E2}$$

for $X=\left(\overline{\kappa}^{(*1)}\sigma\right)^2$. The solution X to eqn (E2) is

$$X=\frac{1}{\alpha_1{}^2-4\alpha_2}\left[\alpha_1+2\alpha_2\mathcal{E}^2-2\sqrt{\alpha_2}(1+\alpha_1\mathcal{E}^2+\alpha_2\mathcal{E}^4)^{1/2}\right]. \tag{E3}$$

At a low field strength of $\mathcal{E}\ll 1$, the numerator on the rhs of eqn (E3) is approximated by

$$\begin{aligned}&\alpha_1+2\alpha_2\mathcal{E}^2-2\sqrt{\alpha_2}(1+\alpha_1\mathcal{E}^2+\alpha_2\mathcal{E}^4)^{1/2}\\ &\approx \alpha_1+2\alpha_2\mathcal{E}^2-2\sqrt{\alpha_2}\left(1+\frac{\alpha_1\mathcal{E}^2}{2}\right)\\ &=(\alpha_1-2\sqrt{\alpha_2})(1-\sqrt{\alpha_2}\mathcal{E}^2),\end{aligned} \tag{E4}$$

whereas we have

$$\begin{aligned}&\alpha_1+2\alpha_2\mathcal{E}^2-2\sqrt{\alpha_2}(1+\alpha_1\mathcal{E}^2+\alpha_2\mathcal{E}^4)^{1/2}\\ &\approx 2\alpha_2\mathcal{E}^2-2\sqrt{\alpha_2}(\alpha_2\mathcal{E}^4)^{1/2}=0,\end{aligned} \tag{E5}$$

for the high field strength of $\mathcal{E}\gg 1$. While the approximate form (E4) of the numerator results in the expression (89), the limiting result (90) is valid due to eqn (E5).

Acknowledgements

The author thanks the anonymous referees for their valuable comments and suggestions.

References

1 (*a*) Y. Levin, *Rep. Prog. Phys.*, 2002, **65**, 1577; (*b*) D. Andelman, Introduction to Electrostatics in Soft and Biological Matter, in *Soft Condensed Matter Physics in Molecular and Cell Biology*, ed. W. C. K. Poon and D. Andelman, CRC Press, 2006.

2 (*a*) H. Bruus, *Theoretical Microfluidics*, Oxford University Press, Oxford, 2007; (*b*) R. B. Schoch, J. Han and P. Renaud, *Rev. Mod. Phys.*, 2008, **80**, 839; (*c*) L. Bocquet and E. Charlaix, *Chem. Soc. Rev.*, 2010, **39**, 1073–1095.

3 (*a*) H. Weingärtner, *Angew. Chem., Int. Ed.*, 2008, **47**, 654–670; (*b*) M. V. Fedorov and A. A. Kornyshev, *Chem. Rev.*, 2014, **114**, 2978–3036; (*c*) R. Hayes, G. G. Warr and R. Atkin, *Chem. Rev.*, 2015, **115**, 6357–6426.

4 (*a*) C. Zhong, Y. Deng, W. Hu, J. Qiao, L. Zhang and J. Zhang, *Chem. Soc. Rev.*, 2015, **44**, 7484–7539; (*b*) T. M. Gür, *Energy Environ. Sci.*, 2018, **11**, 2696–2767.

5 (*a*) M. S. Kilic, M. Z. Bazant and A. Ajdari, *Phys. Rev. E: Stat., Nonlinear, Soft Matter Phys.*, 2007, **75**, 02150; (*b*) B. D. Storey and M. Z. Bazant, *Phys. Rev. E: Stat., Nonlinear, Soft Matter Phys.*, 2012, **86**, 056303; (*c*) T. R. Ferguson and M. Z. Bazant, *J. Electrochem. Soc.*, 2012, **159**, A1967; (*d*) M. Schmuck and M. Z. Bazant, *SIAM J. Appl. Math.*, 2015, **75**, 1369–1401; (*e*) J. P. de Souza, C. M. Chow, R. Karnik and M. Z. Bazant, *Phys. Rev. E*, 2021, **104**, 044802.

6 (*a*) D. Gillespie, W. Nonner and R. S. Eisenberg, *J. Phys.: Condens. Matter*, 2002, **14**, 12129; (*b*) B. Eisenberg, Y. Hyon and C. Liu, *J. Chem. Phys.*, 2010, **133**, 104104; (*c*) T. L. Horng, T. C. Lin, C. Liu and B. Eisenberg, *J. Phys. Chem. B*, 2012, **116**, 11422–11441; (*d*) J. L. Liu and B. Eisenberg, *J. Chem. Phys.*, 2014, **141**, 12B640_1; (*e*) J. L. Liu and B. Eisenberg, *Entropy*, 2020, **22**, 550.

7 (*a*) B. Corry, S. Kuyucak and S. H. Chung, *Biophys. J.*, 2000, **78**, 2364–2381; (*b*) B. Corry, S. Kuyucak and S. H. Chung, *Biophys. J.*, 2003, **84**, 3594–3606; (*c*) Q. Zheng and G. W. Wei, *J. Chem. Phys.*, 2011, **134**, 194101; (*d*) C. Maffeo, S. Bhattacharya, J. Yoo, D. Wells and A. Aksimentiev, *Chem. Rev.*, 2012, **112**, 6250–6284.

8 (*a*) A. Yochelis, *J. Phys. Chem. C*, 2014, **118**, 5716–5724; (*b*) N. Gavish, D. Elad and A. Yochelis, *J. Phys., Lett.*, 2018, **9**, 36–42.

9 (*a*) M. Burger, B. Schlake and M. T. Wolfram, *Nonlinearity*, 2012, **25**, 961; (*b*) A. A. Lee, S. Kondrat, D. Vella and A. Goriely, *Phys. Rev. Lett.*, 2015, **115**, 106101; (*c*) C. Wang, J. Bao, W. Pan and X. Sun, *Electrophoresis*, 2017, **38**, 1693–1705; (*d*) S. Fleischmann, J. B. Mitchell, R. Wang, C. Zhan, D. E. Jiang, V. Presser and V. Augustyn, *Chem. Rev.*, 2020, **120**, 6738–6782; (*e*) S. H. Amrei, G. H. Miller, K. J. Bishop and W. D. Ristenpart, *Soft Matter*, 2020, **16**, 7052–7062; (*f*) M. Schammer, B. Horstmann and A. Latz, *J. Electrochem. Soc.*, 2021, **168**, 026511; (*g*) A. Gupta, P. J. Zuk and H. A. Stone, *Phys. Rev. Lett.*, 2020, **125**, 076001; (*h*) F. Henrique, P. J. Zuk and A. Gupta, *Soft Matter*, 2022, **18**, 198–213.

10 (*a*) Z. Xu, M. Ma and P. Liu, *Phys. Rev. E: Stat., Nonlinear, Soft Matter Phys.*, 2014, **90**, 013307; (*b*) P. Liu, X. Ji and Z. Xu, *SIAM J. Appl. Math.*, 2018, **78**, 226–245; (*c*) M. Ma, Z. Xu and L. Zhang, *SIAM J. Appl. Math.*, 2021, **81**, 1645–1667; (*d*) M. Ma, Z. Xu and L. Zhang, *Phys. Rev. E*, 2021, **104**, 035307.

11 M. te Vrugt, H. Löwen and R. Wittkowski, *Adv. Phys.*, 2020, **69**, 121–247.

12 (*a*) U. M.-B. Marconi, S. Melchionna and I. Pagonabarraga, *J. Chem. Phys.*, 2013, **138**, 244107; (*b*) J. Jiang, D. Cao, D. E. Jiang and J. Wu, *J. Phys.: Condens. Matter*, 2014, **26**, 284102; (*c*) C. Zhan, C. Lian, Y. Zhang, M. W. Thompson, Y. Xie, J. Wu, P. R.-C. Kent, P. T. Cummings, D. Jiang and D. J. Wesolowski, *Adv. Sci.*, 2017, **4**, 1700059; (*d*) H. Gao and C. Xiao, *Europhys. Lett.*, 2018, **124**, 58002; (*e*) S. Babel, M. Eikerling and H. Löowen, *J. Phys. Chem. C*, 2018, **122**, 21724–21734.

13 (*a*) V. Démery and D. S. Dean, *J. Stat. Mech.: Theo. Exp.*, 2016, **2016**, 023106; (*b*) A. Poncet, O. Bénichou, V. Démery and G. Oshanin, *New J. Phys.*, 2017, **118**, 118002.

 This journal is © The Royal Society of Chemistry 2022

Open Access Article. Published on 26 May 2022. Downloaded on 7/19/2025 4:45:38 PM. This article is licensed under a Creative Commons Attribution-NonCommercial 3.0 Unported Licence.

14 (*a*) S. Mahdisoltani and R. Golestanian, *Phys. Rev. Lett.*, 2021, **126**, 158002; (*b*) S. Mahdisoltani and R. Golestanian, *New J. Phys.*, 2021, **23**, 073034.

15 Y. Avni, R. M. Adar, D. Andelman and H. Orland, *Phys. Rev. Lett.*, 2022, **128**, 098002.

16 (*a*) J. P. Péraud, A. J. Nonaka, J. B. Bell, A. Donev and A. L. Garcia, *Proc. Natl. Acad. Sci. U. S. A.*, 2017, **114**, 10829–10833; (*b*) A. Donev, A. J. Nonaka, C. Kim, A. L. Garcia and J. B. Bell, *Phys. Rev. Fluids*, 2019, **4**, 043701; (*c*) A. Donev, A. L. Garcia, J. P. Péraud, A. J. Nonaka and J. B. Bell, *Curr. Opin. Electrochem.*, 2019, **13**, 1–10.

17 (*a*) J. Chakrabarti, J. Dzubiella and H. Löwen, *Phys. Rev. E: Stat., Nonlinear, Soft Matter Phys.*, 2004, **70**, 012401; (*b*) H. Löwen, *Soft Matter*, 2010, **6**, 3133–3142.

18 (*a*) T. Vissers, A. van Blaaderen and A. Imhof, *Phys. Rev. Lett.*, 2011, **106**, 228303; (*b*) M. Ikeda, H. Wada and H. Hayakawa, *Europhys. Lett.*, 2012, **99**, 68005; (*c*) K. Klymko, P. L. Geissler and S. Whitelam, *Phys. Rev. E*, 2016, **94**, 022608; (*d*) C. Reichhardt and C. J.-O. Reichhardt, *Soft Matter*, 2018, **14**, 490–498; (*e*) B. Li, Y. L. Wang, G. Shi, Y. Gao, X. Shi, C. E. Woodward and J. Forsman, *ACS Nano*, 2021, **15**, 2363–2373.

19 (*a*) M. A. Gebbie, H. A. Dobbs, M. Valtiner and J. N. Israelachvili, *Proc. Natl. Acad. Sci. U. S. A.*, 2015, **112**, 7432–7437; (*b*) A. A. Lee, D. Vella, S. Perkin and A. Goriely, *J. Phys. Chem. Lett.*, 2015, **6**, 159–163; (*c*) A. M. Smith, A. A. Lee and S. Perkin, *J. Phys. Chem. Lett.*, 2016, **7**, 2157–2163; (*d*) M. A. Gebbie, A. M. Smith, H. A. Dobbs, G. G. Warr, X. Banquy, M. Valtiner, M. W. Rutland, J. N. Israelachvili, S. Perkin and R. Atkin, *Chem. Commun.*, 2017, **53**, 1214–1224; (*e*) A. A. Lee, C. S. Perez-Martinez, A. M. Smith and S. Perkin, *Phys. Rev. Lett.*, 2017, **119**, 026002; (*f*) P. Gaddam and W. Ducker, *Langmuir*, 2019, **35**, 5719–5727; (*g*) C. S. Perez-Martinez and S. Perkin, *Soft Matter*, 2019, **15**, 4255–4265.

20 (*a*) G. Feng, M. Chen, S. Bi, Z. A. Goodwin, E. B. Postnikov, N. Brilliantov, M. Urbakh and A. A. Kornyshev, *Phys. Rev. X*, 2019, **9**, 021024; (*b*) N. Anousheh, F. J. Solis and V. Jadhao, *AIP Adv.*, 2020, **10**, 125312; (*c*) S. W. Coles, C. Park, R. Nikam, M. Kanduc, J. Dzubiella and B. Rotenberg, *J. Phys. Chem. B*, 2020, **124**, 1778–1786; (*d*) J. Zeman, S. Kondrat and C. Holm, *Chem. Commun.*, 2020, **56**, 15635–15638; (*e*) J. Zeman, S. Kondrat and C. Holm, *J. Chem. Phys.*, 2021, **155**, 204501; (*f*) E. Krucker-Velasquez and J. W. Swan, *J. Chem. Phys.*, 2021, **155**, 134903.

21 M. Z. Bazant, B. D. Storey and A. A. Kornyshev, *Phys. Rev. Lett.*, 2011, **106**, 046102.

22 (*a*) R. P. Misra, J. P. de Souza, D. Blankschtein and M. Z. Bazant, *Langmuir*, 2019, **35**, 11550–11565; (*b*) J. P. de Souza, Z. A.-H. Goodwin, M. McEldrew, A. A. Kornyshev and M. Z. Bazant, *Phys. Rev. Lett.*, 2020, **125**, 116001; (*c*) J. P. de Souza and M. Z. Bazant, *J. Phys. Chem. C*, 2020, **124**, 11414–11421.

23 (*a*) S. Buyukdagli and R. Blossey, *J. Phys.: Condens. Matter*, 2016, **28**, 343001; (*b*) R. Blossey, A. C. Maggs and R. Podgornik, *Phys. Rev. E*, 2017, **95**, 060602; (*c*) C. D. Santangelo, *Phys. Rev. E: Stat., Nonlinear, Soft Matter Phys.*, 2006, **73**, 041512; (*d*) M. M. Hatlo and L. Lue, *Soft Matter*, 2009, **5**, 125–133; (*e*) M. M. Hatlo and L. Lue, *Europhys. Lett.*, 2010, **89**, 25002; (*f*) T. Xiao and X. Song, *J. Phys. Chem. A*, 2021, **125**, 2173–2183.

24 H. Frusawa, *J. Stat. Mech.: Theory Exp.*, 2021, 2021, 013213.

25 (*a*) Z. G. Wang, *Phys. Rev. E: Stat., Nonlinear, Soft Matter Phys.*, 2010, **81**, 021501; (*b*) M. Ma and Z. Xu, *J. Chem. Phys.*, 2014, **141**, 244903; (*c*) R. Wang and Z. G. Wang, *J. Chem. Phys.*, 2015, **142**, 104705; (*d*) R. Wang and Z. G. Wang, *J. Chem. Phys.*, 2016, **144**, 134902; (*e*) H. Frusawa, *Phys. Rev. E*, 2020, **101**, 012121.

26 (*a*) T. Munakata, *J. Phys. Soc. Jpn.*, 1989, **58**, 2434–2438; (*b*) K. Kawasaki, *Physica A*, 1994, **208**, 35–64; (*c*) D. S. Dean, *J. Phys. A: Math. Gen.*, 1996, **29**, L613; (*d*) H. Frusawa and R. Hayakawa, *J. Phys. A: Math. Gen.*, 2000, **33**, L155; (*e*) V. Démery, O. Bénichou and H. Jacquin, *New J. Phys.*, 2014, **16**, 053032; (*f*) P. H. Chavanis, *Entropy*, 2019, **21**, 1006.

27 (*a*) T. Leonard, B. Lander, U. Seifert and T. Speck, *J. Chem. Phys.*, 2013, **139**, 204109; (*b*) H. Jacquin, B. Kim, K. Kawasaki and F. van Wijland, *Phys. Rev. E: Stat., Nonlinear, Soft Matter Phys.*, 2015, **91**, 022130; (*c*) N. Bidhoodi and S. P. Das, *Phys. Rev. E: Stat., Nonlinear, Soft Matter Phys.*, 2015, **92**, 012325; (*d*) D. S. Dean, B. S. Lu, A. C. Maggs and R. Podgornik, *Phys. Rev. Lett.*, 2016, **116**, 240602; (*e*) M. Krüger and D. S. Dean, *J. Chem. Phys.*, 2017, **146**, 134507; (*f*) J. F. Lutsko, *Sci. Adv.*, 2019, **5**, eaav7399; (*g*) L. Tociu, É. Fodor, T. Nemoto and S. Vaikuntanathan, *Phys. Rev. X*, 2019, **9**, 4.

28 (*a*) H. Frusawa, *J. Phys. A: Math. Theor.*, 2019, **52**, 065003; (*b*) H. Frusawa, *Entropy*, 2020, **22**, 34; (*c*) H. Frusawa, *Soft Matter*, 2021, **17**, 8810–8831.

29 (*a*) B. Rotenberg, O. Bernard and J. P. Hansen, *J. Phys.: Condens. Matter*, 2018, **30**, 054005; (*b*) F. Coupette, A. A. Lee and A. Härtel, *Phys. Rev. Lett.*, 2018, **121**, 075501; (*c*) R. Kjellander, *Soft Matter*, 2019, **15**, 5866–5895; (*d*) R. Kjellander, *Phys. Chem. Chem. Phys.*, 2020, **22**, 23952–23985; (*e*) C. W. Outhwaite and L. B. Bhuiyan, *J. Chem. Phys.*, 2021, **155**, 014504; (*f*) A. Ciach and O. Patsahan, 2021, arXiv preprint, arXiv:2102.00878.

30 (*a*) R. M. Adar, S. A. Safran, H. Diamant and D. Andelman, *Phys. Rev. E*, 2019, **100**, 042615; (*b*) Y. Avni, R. M. Adar and D. Andelman, *Phys. Rev. E*, 2020, **101**, 010601.

31 P. Cats, R. Evans, A. Härtel and R. van Roij, *J. Chem. Phys.*, 2021, **154**, 124504.

32 J. G. Kirkwood and J. C. Poirier, *J. Phys. Chem.*, 1954, **58**, 591–596.

33 (*a*) P. Attard, *Phys. Rev. E: Stat., Nonlinear, Soft Matter Phys.*, 1993, **48**, 3604; (*b*) J. Ennis, R. Kjellander and D. J. Mitchell, *J. Chem. Phys.*, 1995, **102**, 975; (*c*) B. P. Lee and M. E. Fisher, *Europhys. Lett.*, 1997, **39**, 611; (*d*) O. Patsahan and A. Ciach, *J. Phys.: Condens. Matter*, 2007, **19**, 236203; (*e*) J. Janecek and R. R. Netz, *J. Chem. Phys.*, 2009, **130**, 074502.

34 P. B. Warren and A. Vlasov, *J. Chem. Phys.*, 2014, **140**, 084904.

Open Access Article. Published on 26 May 2022. Downloaded on 7/19/2025 4:45:38 PM.
This article is licensed under a Creative Commons Attribution-NonCommercial 3.0 Unported Licence.

35 (*a*) P. B. Warren, A. Vlasov, L. Anton and A. J. Masters, *J. Chem. Phys.*, 2013, **138**, 204907; (*b*) D. Frydel, *J. Chem. Phys.*, 2016, **145**, 184703; (*c*) D. Frydel and M. Ma, *Phys. Rev. E*, 2016, **93**, 062112.
36 (*a*) R. J.-F. Leote de Carvalho and R. Evans, *Mol. Phys.*, 1994, **83**, 619–654; (*b*) A. J. Archer, D. Pini, R. Evans and L. Reatto, *J. Chem. Phys.*, 2007, **126**, 014104.
37 (*a*) R. Evans, *Adv. Phys.*, 1979, **28**, 143–200; (*b*) J. Wu, *AIChE J.*, 2006, **52**, 1169–1193; (*c*) J. Wu and Z. Li, *Annu. Rev. Phys. Chem.*, 2007, **58**, 85–112.
38 T. V. Ramakrishnan and M. Yussouff, *Phys. Rev. B: Condens. Matter Mater. Phys.*, 1979, **19**, 2775.
39 D. Frydel, *Adv. Chem. Phys.*, 2016, **160**, 209–260.
40 (*a*) Y. G. Chen, C. Kaur and J. D. Weeks, *J. Phys. Chem. B*, 2004, **108**, 19874; (*b*) Y. G. Chen and J. D. Weeks, *Proc. Natl. Acad. Sci. U. S. A.*, 2006, **103**, 7560.
41 (*a*) H. Frusawa, *Phys. Rev. E*, 2018, **98**, 052130; (*b*) N. V. Brilliantov, J. M. Rubí and Y. A. Budkov, *Phys. Rev. E*, 2020, **101**, 042135; (*c*) Y. A. Budkov, *Phys. Chem. Chem. Phys.*, 2020, **22**, 14756–14772.
42 K. C. Ng, *J. Chem. Phys.*, 1974, **61**, 2680.
43 (*a*) L. M. Varela, M. Perez-Rodriguez, M. Garcia, F. Sarmiento and V. Mosquera, *J. Chem. Phys.*, 1999, **111**, 10986–10997; (*b*) L. M. Varela, M. Garcia and V. Mosquera, *Phys. Rep.*, 2003, **382**, 1–111; (*c*) L. M. Varela, M. Perez-Rodriguez, M. Garcia, F. Sarmiento and V. Mosquera, *J. Chem. Phys.*, 1998, **109**, 1930–1938.
44 M. E. Fisher and B. Wiodm, *J. Chem. Phys.*, 1969, **50**, 3756–3772.
45 H. Frusawa, *Entropy*, 2022, **24**, 500.
46 (*a*) T. Singh and A. Kumar, *J. Phys. Chem. B*, 2008, **112**, 12968–12972; (*b*) A. Rybinska-Fryca, A. Sosnowska and T. Puzyn, *J. Mol. Liq.*, 2018, **260**, 57–64.
47 (*a*) R. Shi and Y. Wang, *J. Phys. Chem. B*, 2013, **117**, 5102–5112; (*b*) Y. L. Wang, B. Li, S. Sarman, F. Mocci, Z. Y. Lu, J. Yuan, A. Laaksonen and M. D. Fayer, *Chem. Rev.*, 2020, **120**, 5798–5877.

 This journal is © The Royal Society of Chemistry 2022